CRUSTAL SRUCTURE IN CENTRAL AND NORTHERN TAIWAN FROM RECEIVER FUNCTIONS

A Thesis

Presented to the Faculty of the Graduate School

of Cornell University

In Partial Fulfillment of the Requirements for the Degree of

Master of Science

by

Danielle Glasgow Wolf

January 2012

ABSTRACT

Taiwan is the type-example of arc-continent collision, with the Luzon Arc on the oceanic Philippine Sea Plate (PSP) colliding with the continental margin of the Eurasian Plate (EUP). In this three-dimensionally complex convergence zone, the PSP subducts to the north beneath the EUP off of northeastern Taiwan, while the EUP subducts to the east beneath the PSP in central and southern Taiwan. The resulting accretion of the Philippine arc crust to the Eurasian continental margin exemplifies an important process in the growth of continents, yet the geometry and structure of the lithosphere at depth are poorly constrained. Some models of the Taiwan orogen propose that thin-skinned deformation above a basal décollement is the dominant deformational style, while other models suggest lithospheric-scale deformation and crustal thickening. This study, conducted as part of the TAiwan Integrated GEophysical Research (TAIGER) project, uses P and S wave receiver functions calculated from teleseismic earthquake data recorded at 30 broadband seismic stations deployed across northern and central Taiwan to detect lithospheric structure and further constrain the style of deformation at the Taiwan orogen.

P wave receiver functions suggest the presence of a detachment fault in western central Taiwan continuing eastward from the Western foothills through the Hsueshan Range, and past the Lishan Fault into the Western Central Range. In central Taiwan, P and S wave receiver functions indicate that the crust thickens to the east, with estimated Moho depths increasing from approximately 29 km on the western coast to ~50 km beneath the Central Ranges. On the western coast of northern Taiwan, receiver functions yield an estimated Moho depth of approximately 23 km, with Moho depths increasing to ~40 – 45 km beneath north-central Taiwan. S wave receiver functions indicate that the depth to the base of the Eurasian slab beneath central

Taiwan increases from ~100 km beneath the Coastal Plain in the west to ~165 km beneath central Taiwan. The base of the PSP lithosphere beneath eastern central Taiwan is estimated at ~120 km. These new estimates of crustal structure imply thin-skinned deformation above a crustal-scale detachment in western Taiwan, with a transition to thicker crust and thick-skinned deformation in central and eastern Taiwan beneath the Hsueshan and Central Ranges.

BIOGRAPHICAL SKETCH

Danielle is the daughter of Jan Piper-Glasgow and Andrew Glasgow. She was born and raised in Victor, New York, and has two younger brothers, Nathan and Alexander Glasgow. Danielle attended Boston University as an undergraduate and earned a Bachelor of Arts in Earth Sciences in 2004 after studying geology abroad in New Zealand and Ireland. Danielle came to Cornell University in the fall of 2005, where she met and later married fellow graduate student David Wolf. While at Cornell, Danielle also completed a Masters in the Art of Teaching and plans to pursue employment as an Earth Science teacher. Danielle and David relocated to Houston, Texas with their two dogs after completing their graduate studies in Ithaca.

ACKNOWLEDGMENTS

This thesis would not have been possible without the education and guidance that I received from both my primary advisor, Larry D. Brown, and my minor advisor, Richard W. Allmendinger. I offer my thanks to them both for their continued encouragement and patience throughout this process. My gratitude also goes out to the whole TAIGER team for the wealth of knowledge and experience they have shared with me, particularly Francis Wu (Binghamton University), David Okaya (University of Southern California), C.Y. Wang (National Central University, Taiwan), B.S. Huang (Institute for Earth Sciences, Academia Sinica, Taiwan), Eleanor Sonley (Binghamton University), Hao Kuo-Chen, and En-Jui "Rick" Lee (Binghamton University). This work was supported through grant EAR-0410227 from the National Science Foundation. I would further like to acknowledge the rest of the faculty in the Department of Earth & Atmospheric Sciences at Cornell University, with a special nod to Muawia Barazangi and all his C minuses.

I would also like to thank the members of the Cornell EAS community, especially my fellow graduate students, who provided valuable insight, support, and encouragement during my time at Cornell. Extra special thanks goes to Tiffany Tchakirides, Holly Moore, Phoebe Judge, Naomi Kirk-Lawlor, and Amanda Baker—you were the ones that I could always count on, no matter what kind of academic or emotional support I needed. I may have been able to do this without you, but I wouldn't have had nearly as much fun along the way.

Neil McGlashan deserves much gratitude for answering endless questions about software and methods with unfailing good humor and for knowing who to ask when we couldn't find the answer on our own. Steve Gallow came to my rescue more than once by patiently helping me through a wide variety of computer hang-ups; thank

you, Steve. And in the EAS office, Judy Starr and Savannah Sawyer worked wonders to make the administrative details go as smoothly as possible.

Finally, I owe immeasurable gratitude to my parents, who never failed to listen and to give sage advice during this sometimes-rocky trip, and to David Wolf, who stood firmly by my side the whole way. Much love—I can't thank you enough.

TABLE OF CONTENTS

LIST OF FIGURES

LIST OF TABLES

LIST OF ABBREVIATIONS

EUP	Eurasian Plate
IRIS	Incorporated Research Institutions for Seismology
LAB	Lithosphere-Asthenosphere Boundary
PRF	P wave Receiver Function
PSP	Philippine Sea Plate
RCRF	Ray Coordinate Reference Frame
SRF	S wave Receiver Function
TAIGER	TAiwan Integrated GEodynamic Research
USGS	United States Geological Survey

LIST OF SYMBOLS

(φ_0, λ_0)	Latitude and longitude of a seismic station
(φ, λ)	Latitude and longitude of an earthquake epicenter
Δ	Angular distance, in degrees, between seismic station and epicenter
α	Azimuth, in degrees, from station to epicenter
i	Angle of incidence of up-going seismic wave
p	Seismic ray parameter
v	Seismic velocity
H	Depth from surface to seismic discontinuity
t_{ps}	Difference in the arrival times of the P and the converted Ps phases
Vp	P wave velocity
Vs	S wave velocity

LIST OF FORMULAE

(1) $$H = t_{ps} / [(1 / Vs^2 - p^2)^{1/2} - (1 / Vp^2 - p^2)^{1/2}]$$

TECTONICS OF THE TAIWAN OROGEN

Tectonic Setting

At the Taiwan collision zone, the eastward subduction of the Eurasian plate continental margin beneath the Luzon Arc on the oceanic Philippine Sea Plate (see Figure 1) makes Taiwan a prime example of arc-continent collision. Arc-continent collision and the subsequent accretion of volcanic terranes are two of the primary processes involved in the growth of continents and both of these processes are currently occurring at the Taiwan orogen. Study of the Taiwan collisional system can help to expand our understanding of the nature of these important processes.

The southeastern Eurasian plate (EUP) is predominantly comprised of continental crust, with a transition to rifted continental margin and to oceanic crust in the southeast (Bowin et al., 1978; Taylor and Hayes, 1983). The Philippine Sea plate (PSP) is composed of oceanic crust and is marked on its western edge by the Luzon Arc, which was formed by the eastward subduction of oceanic EUP beneath the PSP. This arc-continent collision began approximately 8 Ma (Ho, 1988; Kao et al., 1998; Lallemand et al., 2001; Teng, 1990). Off the east coast of central and northern Taiwan, this subduction geometry is reversed and the PSP subducts to the north beneath the EUP, forming the Ryukyu trench and arc (Angelier, 1986; Chai, 1972). The dual subduction geometry at the Taiwan orogen complicates the Moho topography in the region surrounding northern Taiwan and necessitates a tear fault in the down-going Eurasian plate (Lallemand et al., 1997).

The convergence between the two plates is described as movement of the PSP to the northwest at ~81 mm/year with respect to a fixed EUP (Yu et al., 1997; Yu et al., 1999). In combination with the northeast-southwest trend of the EUP-PSP boundary, this plate motion results in oblique collision between the Luzon Arc and the

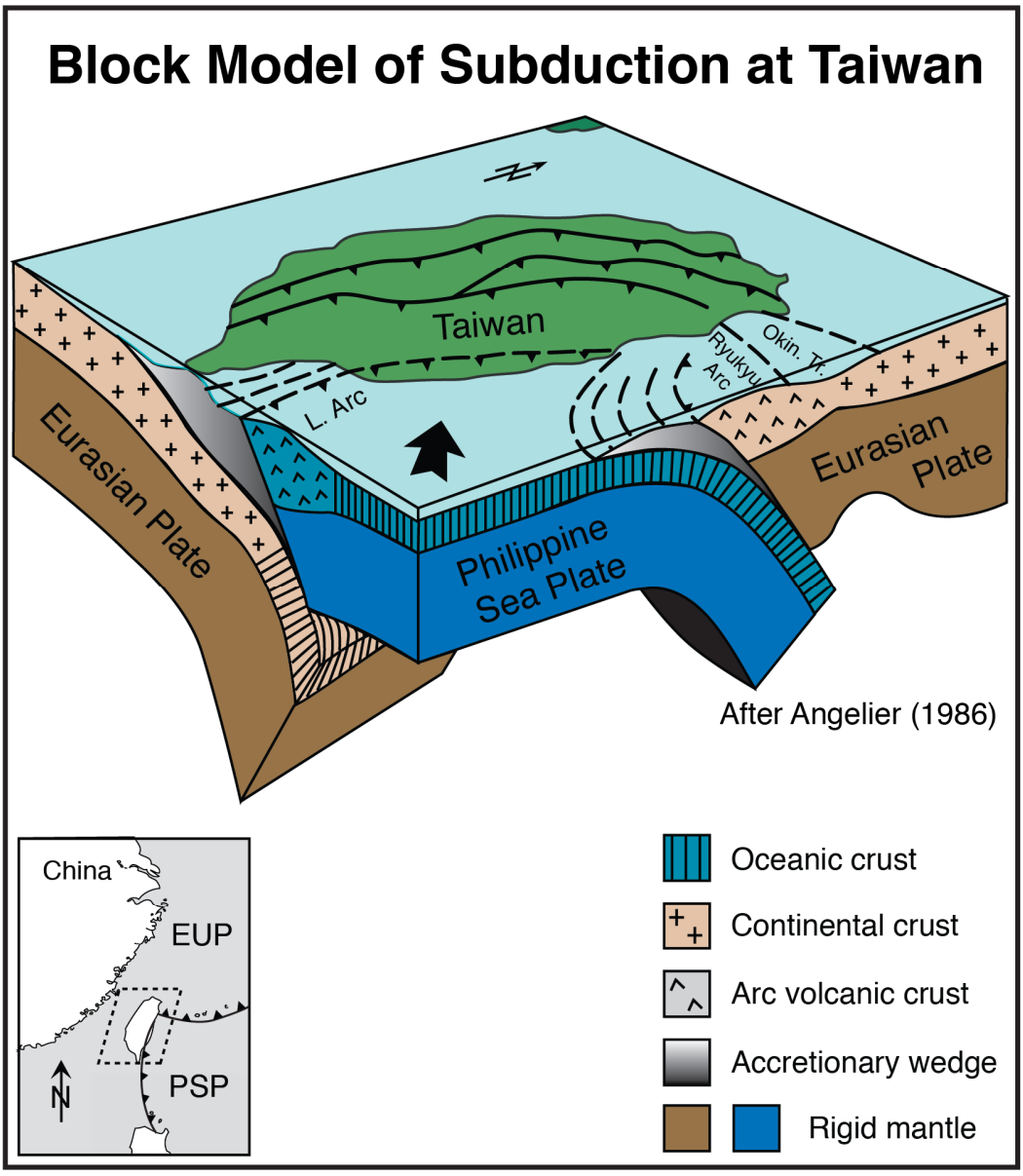

Figure 1. Block model illustrating dual subduction geometries at Taiwan after Angelier (1986). In central and southern Taiwan, the Eurasian continental margin collides with the Luzon Arc on the Philippine Sea Plate, while in northeastern Taiwan, the Philippine Sea Plate subducts beneath the Eurasian Plate.

Eurasian continental margin. This causes southwestward propagation of arc-continent collision and estimated shortening of the EUP continental margin by approximately 160 to 200 km (Suppe, 1981). Collision extends along the plate boundary to the south, incorporating more of the Luzon arc and EUP continental margin with time (Lewis and Hayes, 1983; Suppe, 1981).

The bedrock of Taiwan is composed predominantly of sedimentary and meta-sedimentary rock derived from the Chinese continental margin (Figure 2). Major lithologies include the slates and schists of the Western Foothills and the higher-grade metamorphic rocks of the Hsueshan and Central Ranges (Chai, 1972; Ho, 1986). In contrast, the volcanic and meta-volcanic rocks of the Coastal Range on Taiwan's southeastern shore are interpreted as an accreted suite from the North Luzon Arc (Chai, 1972; Ho, 1986). The Longitudinal Valley, which separates the Coastal Range from the Central Range and western Taiwan, is generally recognized as the suture zone between the EUP and the PSP (Barrier and Angelier, 1986; Biq, 1972).

Two contrasting models have been proposed to explain crustal deformations in Taiwan resulting from this arc-continent collision. In the thin-skinned model, rocks of the upper crust (10 – 15 km) are transported above a shallow thrust detachment, or décollement, resulting in fold-and-thrust belt geometries (Suppe, 1981; Suppe and Namson, 1979). This process is driven by critical-taper wedge mechanics, and was first described from the rocks of Taiwan's Hsueshan and Central Ranges and the fold-and-thrust belt of the Western Foothills (Barr and Dahlen, 1989; Barr et al., 1991; Dahlen et al., 1984; Davis et al., 1983). In the thin-skinned model, deformation is restricted to the crust above the detachment, and crustal thickening should not significantly impact the Moho morphology, as shown in Figure 3(a).

Other models propose that deformation occurs throughout the entire thickness of the crust. In these "thick-skinned" models, deep structures accommodate

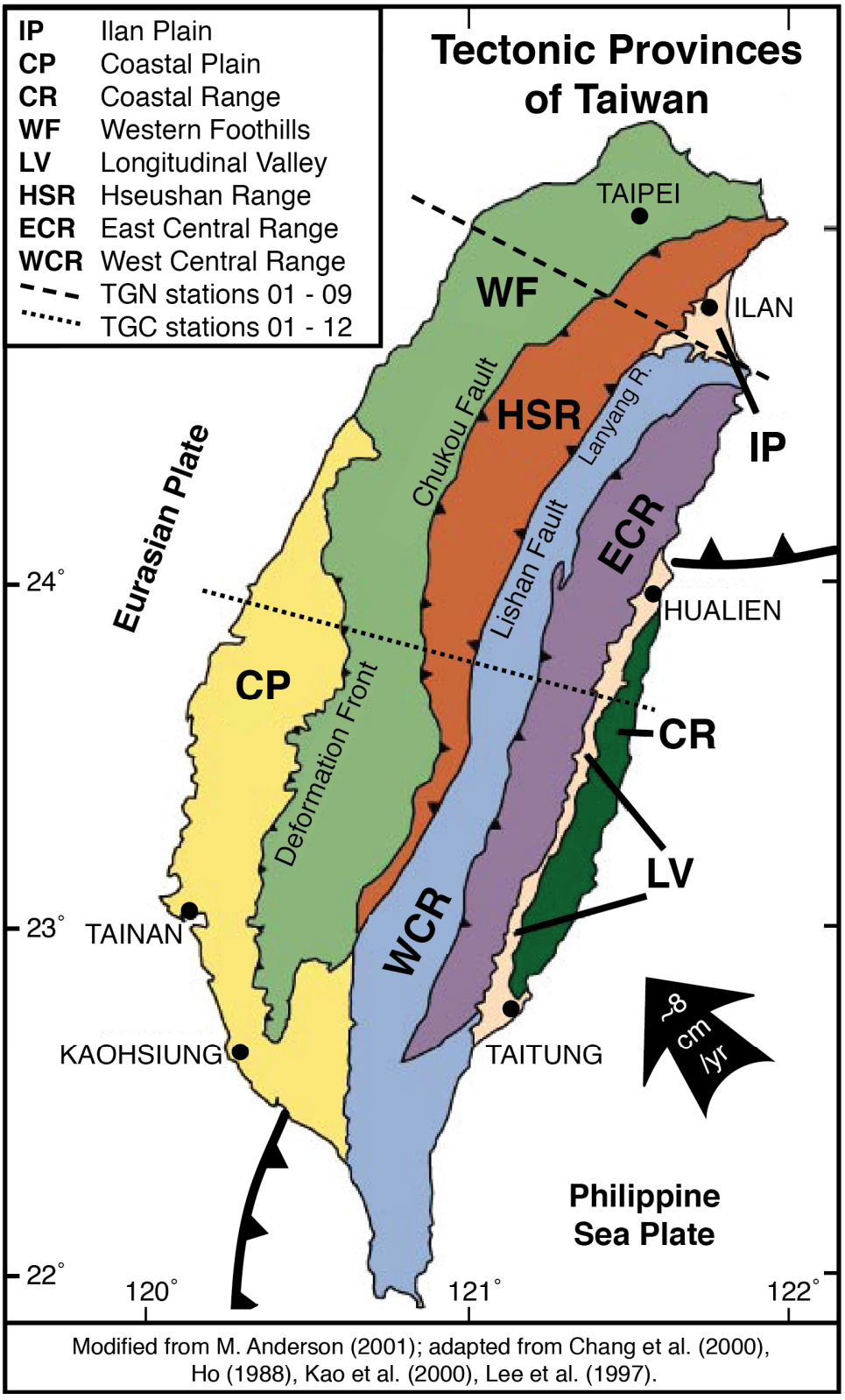

Modified from M. Anderson (2001); adapted from Chang et al. (2000), Ho (1988), Kao et al. (2000), Lee et al. (1997).

Figure 2. Map of the major geologic provinces on the island of Taiwan. From west to east: the Coastal Plan (CP), Western Foothills (WF), Hsueshan Range (HSR), Ilan Plain (IP), West Central Range (WCR), East Central Range (ECR), Longitudinal Valley (LV), and the Coastal Range (CR). The Coastal Plain rocks are predominantly sedimentary, while the bedrock of the Western Foothills and the Hsueshan and Central Ranges is composed of meta-sedimentary rocks, with metamorphic grade increasing towards the center of the orogen. The Coastal Ranges are composed of volcanic and meta-volcanic rocks from the accretion of the North Luzon Arc.

Proposed Collisional Models for the Taiwan Orogen

(a)

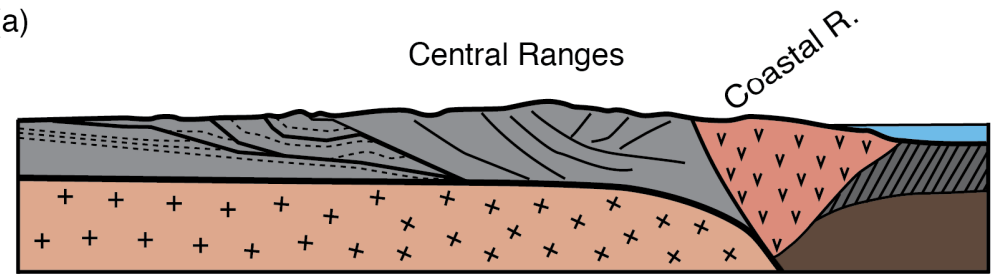

Expanded from Carena et al., 2002

Sedimentary & metased. crust
Volcanic & metavolcanic crust
Crystalline basement
Ocean
Oceanic crust
Rigid mantle

(b) Note: Surface topography has been vertically exaggerated in this section

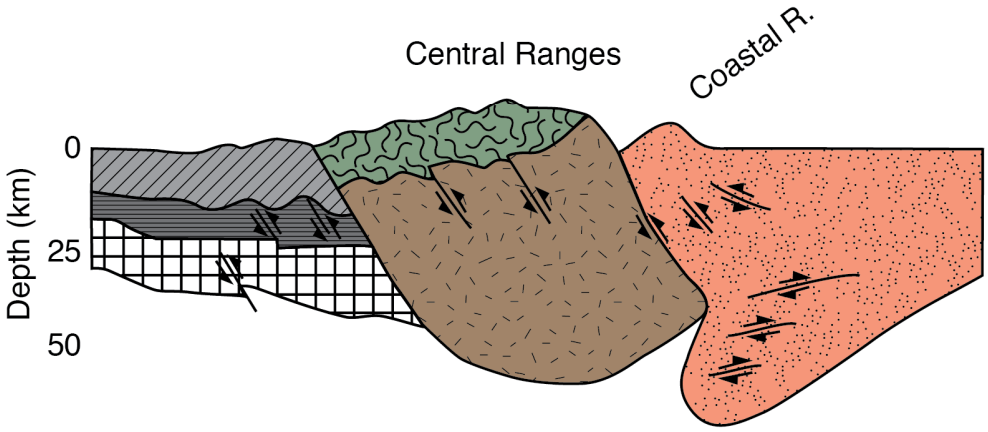

Neogene sedimentary rock
Pre-Tertiary basement
Aseismic crust
Paleogene metased. rock
Crystalline lower crust
Oceanic crust

Modified from Wu et al., 1997

Figure 3. Proposed collisional models for the Taiwan orogen. (a) Thin-skinned collisional model, after Carena et al. (2002). The heavy black line at ~10km depth marks the décollement, with crustal deformation occurring above this fault. Individual thrust sheets are indicated for the Western Foothills on the left side of the cross section. The structure in the Hsueshan and Central Ranges is drawn schematically. In this model, crustal thickening is limited and is the result of imbricated thrust sheets. (b) Lithosphere-involved collisional model from Wu et al. (1997). In this model, faulting and deformation occur throughout the full thickness of the lithosphere, and significant thickening occurs, especially beneath the Hsueshan and Central Ranges. Note that the surface topography has been exaggerated in this section.

displacement by bringing rocks from the lower crust to higher structural levels through a high throw/heave ratio (e.g. Coward, 1983). One such model, shown in Figure 3(b), has been proposed for Taiwan by Wu et al. (1997), citing tomographic evidence for thickened crust in Taiwan's Central Range, the presence of mid- to lower-crustal high-velocity rock, and active seismicity to depths of 60 km. Physical modeling of the orogenic system by Chemenda et al. (2001) similarly suggests that deformation penetrates the crustal lithosphere at the Taiwan orogen, with failure and thickening in the Eurasian continental margin and subsequent uplift and exhumation to form the Central Ranges.

The relative role of thin- versus thick-skinned deformation is an issue in many other orogenic belts, including: the western North American Cordillera, the Appalachians, and the Himalayas, among others. For example, convergence between the North American and Pacific plates, from the Cretaceous through Eocene, has resulted in the development of an expansive cordillera with varying kinematics. In the northern and easternmost Canadian Rockies, deformation is predominately accommodated through the development of fold-thrust belts above basal décollements, with deformation confined to the upper 10-15 km of crust (Armstrong, 1968). In regions of Wyoming, Colorado, Utah, and Nevada, this convergence is accommodated through basement-involved uplift along steeply dipping faults that involve the entire crustal thickness, and is considered to be thick-skinned (Keefer and Love, 1963). This variance in geometry and kinematics is the major defining characteristic between the Sevier (thin-skinned) and Laramide (thick-skinned) orogenies (Armstrong, 1968).

On an even larger scale is the question of sub-crustal deformation during collision. The depth to the base of the lithosphere affected by collision, not only as one plate subducts beneath another, but potentially as one or both plates is deformed and thickened during collision. S wave receiver functions can provide estimates on the

depth to the base of the lithosphere and can help to resolve the degree and extent to which the lithosphere may have been thickened as a result of collision.

The TAIGER Project

Data used in this study were collected as part of the NSF-funded TAiwan Integrated GEodynamic Research (TAIGER) project. The TAIGER project utilizes numerous geophysical techniques to investigate the Taiwan arc-continent collisional system, including: onshore and offshore active-source seismology; land-based broadband and ocean-bottom seismic studies; seismic tomography; and magnetotellurics (Okaya et al., 2009). Geologic mapping, structural analyses, petrophysical measurements, geodynamic modeling, and GPS data analysis were also included in the TAIGER project. Investigators from the following North American institutions participated in the TAIGER project: Binghamton University, Cornell University, Rensselaer Polytechnic Institute, the University of Alberta, the University of Southern California, the University of Texas at Austin, and the University of Wisconsin – Madison. Researchers from the following Taiwanese institutions were also key participants in the TAIGER project: the Institute of Earth Sciences, National Central University, National Chung Cheng University, National Cheng Kung University, National Taiwan Ocean University, and National Taiwan University. The data used in this study was collected during the onshore broadband seismic component of the TAIGER project. Key participants in this component of the TAIGER research group include: Francis Wu from Binghamton University, B.S. Huang from the Institute of Earth Sciences, K.F. Ma and H.Y. Yen from National Central University, Y.M. Wu from National Taiwan University, C.H. Chen from National Chung Cheng University, and R.J. Rau from National Cheng Kung University.

The TAIGER broadband seismic array, deployed throughout Taiwan between September 2006 and May 2008, provided a new pool of seismic data suitable for receiver function analyses. The P and S wave receiver functions from seismic stations in northern and central Taiwan were used to estimate depths to the Moho across the orogen, and S-wave receiver functions were computed to provide estimates on the depth to the lithosphere-asthenosphere boundary (LAB). By analyzing how the depths of these boundaries vary across the zone of collision, we may infer the degree of crustal thickening and make observations about the thickness of the subducting Eurasian slab. Receiver functions may also be sensitive to other crustal discontinuities, and thus might constrain the eastward extent of the décollement seen in the Western Foothills of Taiwan. Previous receiver function studies from other seismic networks on Taiwan were performed on data from only a handful of seismic stations, providing sparse coverage of this complex orogen (e.g. Kim et al., 2004). In this study, data from more than 30 TAIGER seismic stations are analyzed, providing a more complete picture of the plate morphologies in central and northern Taiwan.

The TAIGER stations were deployed in three groups (Figure 4), though data from only the central and northern groups are analyzed in this study for reasons described below. All stations consisted of Güralp Systems Ltd CMG-3T seismometers, operating with a sampling rate of 50 Hz and used in conjunction with Refraction Technology RT-130 3-channel data loggers. The central group, which consisted of twelve stations, was deployed along major east-west highways in central Taiwan at approximately 24°N. The northern group consisted of nineteen stations deployed in two subgroups: as an east-west trending transect at approximately 25°N and as a more distributed network in northeastern Taiwan (see Figure 4). The stations positioned as east-west trending transects are roughly parallel to the direction of plate convergence, making it possible to build cross-sections from the receiver function data

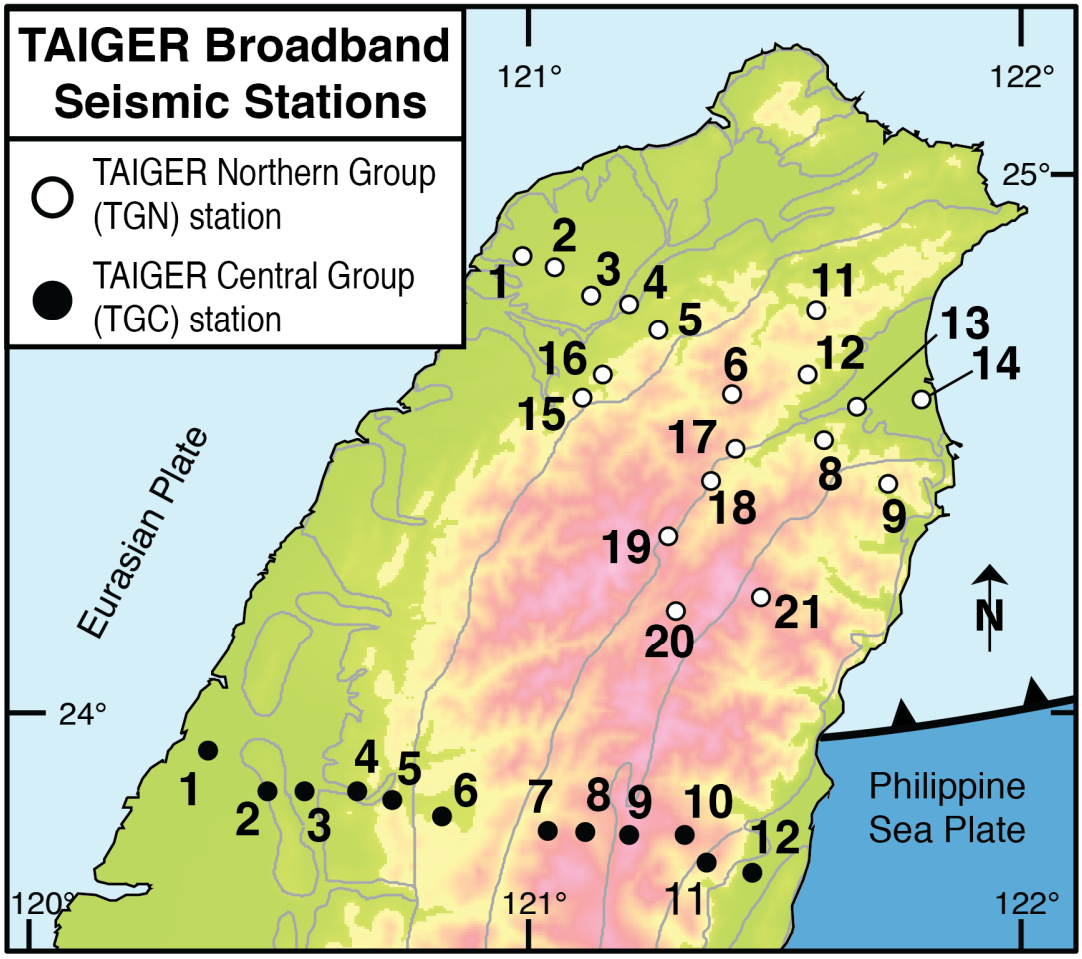

Figure 4. Map of the TAIGER project broadband seismic stations. The northern group (TGN) stations are plotted as open circles, and the central group (TGC) stations are plotted as filled circles.

that focus on: subduction zone geometry, the extent of crustal thickening, and other potential discontinuities resulting from collision.

Data from stations in the southern group, which were also deployed as an east-west trending transect, were judged insufficient for these types of analyses and are not included in this study. Stations in the southern group were deployed after those in the northern and central groups, were serviced less frequently, and were exceptionally noisy. Very few suitable earthquakes were recorded at stations in the southern group with some stations providing no usable data.

METHODS

Receiver Function Technique

The receiver function method utilizes converted seismic waves to constrain the depths of major velocity discontinuities beneath a given receiver, or seismic station. Up-going teleseismic energy encounters velocity discontinuities such as the lithosphere-asthenosphere boundary and the Moho as it radiates away from the earthquake hypocenter. As the seismic waves pass through these discontinuities, a fraction of the energy undergoes a phase conversion; P phases are converted to s phases, and similarly S phases are converted to p phases (Figure 5). Given that the converted phases have different velocities from their parent phases, they arrive either later (P to s) or earlier (S to p) than the parent phases in the seismic wavetrain. By determining the difference in the arrival times of these phases and employing a velocity model, it is possible to estimate the depth of the discontinuity using the following equation:

$$H = t_{ps} / [(1 / Vs^2 - p^2)^{1/2} - (1 / Vp^2 - p^2)^{1/2}] \quad (1)$$

where H is the depth to the discontinuity, t_{ps} is the difference in time between the P arrival and the converted Ps phase, Vs is the S wave velocity, Vp is the P wave velocity, and p is the ray parameter (Al-Damegh et al., 2005). P wave velocity values used in this study were based on the 3D seismic velocity model developed by Font et al. (2003), with an estimated average crustal P wave velocity of 6.37 km/s for the Taiwan orogen. S wave velocity values were estimated using Vp / Vs ratios published by Wu et al. (2007) and are consequently dependent on the Vp values used. A weighted average Vp / Vs ratio of 1.737 was used from 0 to 35 km depth, with a

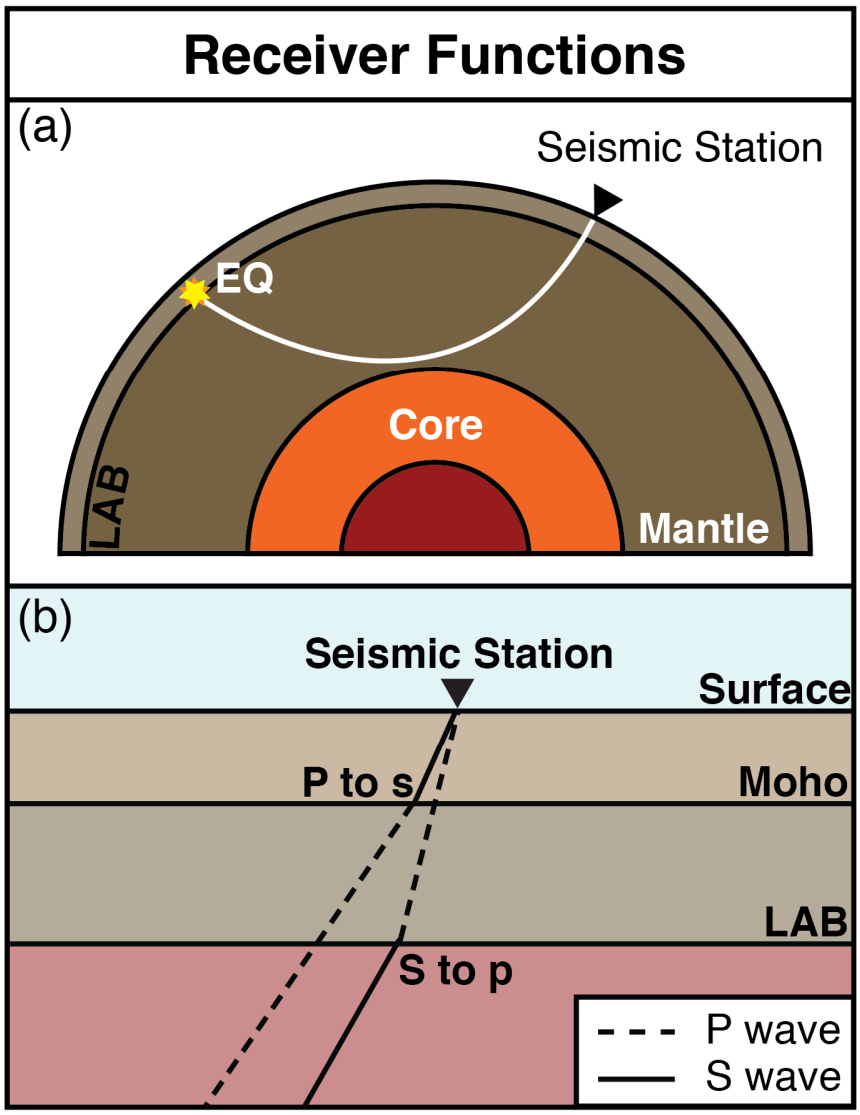

Figure 5. (a) Sketch cross section of the Earth, showing hypothetical locations of a seismic station and a suitable seismic event for receiver function analysis. (b) At major velocity interfaces within the Earth, seismic waves may be converted from one phase to another as they cross the boundary. Examples of a P to s conversion at the Moho and an S to P conversion at the Lithosphere-Asthenosphere Boundary (LAB) are shown. P wave phases are plotted as dashed lines and S wave phases as solid lines.

corresponding average Vs of 3.67. From 35 to 110 km depth, an average Vp of 7.37 km/s was used, based on the IASP-91 reference velocity model (Kennett & Engdahl, 1991). An average Vp / Vs value of 1.734 (Wu et al., 2007) resulted in a calculated average Vs of 4.25 km/s. Ray parameters were calculated via the TauP software suite (Crotwell et al., 1999).

The P wave receiver function (PRF) technique has been widely used to estimate Moho depths in various tectonic settings (Ammon, 1991; Kind and Vinnik, 1988; Langston, 1978; Yuan et al., 1997). In typical receiver function analyses, the Moho is associated with the significant seismic velocity contrast at the base of the crustal column, or more specifically, where the change in seismic velocity from ~6.5 km/s to greater than 8 km/s occurs over less than 1 km of vertical distance (Burdick and Langston, 1977). Investigation of Moho depths beneath Taiwan in this study helps to constrain the extent of thickening of the Eurasian crust at the plate boundary.

Although the PRF technique can provide useful insight into crustal structures, the multiple P wave reverberations that follow the initial P arrival often mask the arrival of converted P to s phases. These reverberations make it difficult or impossible to identify deeper discontinuities such as the LAB. As the converted S to p phase arrives earlier in the wave-train than the main S phase, S to p conversions are free of such reverberations, allowing identification of converted phases from deeper discontinuities and more complex structures (e.g. Kumar et al., 2007). Both types of receiver functions are employed in this study, with the results from the S wave receiver function (SRF) analyses serving as an independent check on the PRF Moho depths as well as providing some constraint on LAB morphology.

P wave receiver functions utilize teleseismic events occurring between 35° and 85° from the station. Beyond this range, incident rays do not arrive at angles steep enough for conversion or the converted phases may be overprinted by surface

reflections and reverberations. S wave receiver functions utilize events that are between 55° and 85° distant. For SRFs, events closer than ~55° are excluded as phases converted at the lithosphere-asthenosphere boundary are not observable due to over-critical incidence (Yuan et al., 2006). Beyond ~85°, SKS phases arrive earlier than the main S-phase, obscuring the S to p conversion so that events with epicentral distances greater than ~85° must also be excluded (Yuan et al., 2006). For consistency, the same pool of events was used for both the PRF and SRF analyses even though PRF analyses are possible over a wider range of azimuths. Because very few suitable events identified between 35° and 55° were present in the dataset, the exclusion of these events from the PRF dataset does not significantly impair the results.

Given the long distances through which the seismic energy must propagate, earthquakes of large magnitude are preferable for both PRFs and SRFs so that sufficient energy is received and recorded at the seismic stations. Although the standard lower bound for source events is typically $M_w \geq 6.0$, when events of this size are scarce, events with magnitudes as low as $M_b \geq 5.0$ may also be included to boost the dataset (e.g. Angus et al., 2009). These smaller magnitude events are not fundamentally different from the events of higher magnitude though they are sometimes more difficult to analyze. For events less than M_w 5.5 recorded at the TAIGER stations, the signals from converted phases are simply not strong enough to be identified with any reliability. A full list of the seismic events used in this study is given in Table 1. The level of background noise at a given station also impacts the size of the seismic event that may be used, as the signal from smaller events can be lost at noisy stations if noise-reduction filtering compromises the seismic signal strength or fidelity.

Table 1. Earthquakes used for P to s and S to p receiver function analyses with the TAIGER broadband dataset. The earthquakes are listed in chronological order, and seismic moment and/or a measure of the earthquakes' magnitude is given wherever data were available. All information is taken from the IRIS catalog. In the far right column, values followed by an asterisk (*) are body wave magnitudes.

Event Name	Date (yyyy/mm/dd)	Time (hh:mm:ss.s)	Latitude	Longitude	Depth (km)	Moment Magnitude
AA	2006/09/03	04:26:29.7	-21.76	-175.15	37	5.9
AB	2006/09/03	22:57:30.7	-24.05	178.82	568	5.9
AD	2006/09/19	13:29:54.3	-26.08	-175.58	17	5.7
B	2006/09/28	06:22:11.9	-16.55	-172.05	44	6.9
C	2006/10/08	13:50:24.6	-23.60	-175.40	10	5.7
AJ	2006/11/30	11:33:26.4	-21.30	-174.79	90	6.0
AM	2006/12/17	12:51:11.9	-21.23	-174.44	31	5.8
G	2007/01/08	20:52:21.3	-18.49	-177.91	408	6.3
J	2007/01/31	03:15:55.7	-29.59	-177.93	54	6.4
AP	2007/02/05	09:56:00.0	-20.62	-175.65	77	5.7
AQ	2007/02/05	10:16:24.4	-20.66	-175.46	15	5.6*
AR	200702/15	10:27:31.2	-32.07	-177.67	34	5.7*
AT	2007/02/25	20:47:27.5	-29.18	-177.16	19	5.5*
AX	2007/03/12	09:59:03.2	-21.05	169.83	69	5.8
K	2007/03/25	00:40:02.7	-20.60	169.41	35	7.1
L	2007/03/25	01:08:19.6	-20.79	169.40	35	6.9
AZ	2007/03/25	21:57:09.3	-20.88	169.01	35	5.5*
BA	2007/03/28	08:08:08.5	-30.76	-178.09	35	5.7*
BB	2007/03/31	21:55:29.1	-20.57	169.22	35	5.5*
M	2007/05/06	21:11:52.9	-19.40	-179.34	679	6.2*
N	2007/05/06	22:01:10.7	-19.21	-179.45	705	6.1
BF	2007/05/07	20:32:32.3	-21.21	-178.62	550	5.7
BG	2007/05/13	11:26:42.2	-19.36	-179.36	652	5.8
BH	2007/05/17	19:29:10.2	-30.60	-178.22	35	5.9
BI	2007/05/27	18:12:35.0	-20.05	-174.53	7	5.8
BL	2007/07/06	17:40:54.8	-16.30	-172.82	45	5.8
BM	2007/07/27	14:46:32.2	-21.45	170.88	35	5.9*
P	2007/08/18	12:32:20.4	-22.19	174.72	35	6.0
Q	2007/08/26	12:37:31.8	-17.30	-174.45	130	6.1
BQ	2007/08/27	17:12:00.0	-17.33	-172.30	10	5.7
R	2007/09/25	05:15:59.9	-30.92	179.89	400	6.2

Suitable teleseismic events for receiver function analysis were identified using the USGS and IRIS databases. All events of $M_w \geq 5.5$ that were located within the appropriate distance range from Taiwan were extracted from the dataset, although non-uniform data recovery in the TAIGER broadband seismic stations meant that records for some events were not available at all stations. The number of events recorded by a given station is affected by both the date on which the station was installed and how frequently it was serviced. If a station was not serviced frequently enough, data loss occurred as disk space on the data logger filled up. Excessive noise at some stations further limited the dataset.

Due to the fact that individual receiver functions are stacked in accordance with piercing point proximity, the pool of suitable events was restricted to those azimuths with an acceptable number of events for stacking (Kumar et al., 2005a; Kumar et al., 2005b; Li et al., 2004). Although suitable teleseismic events occurred across a variety of azimuths, the only region with a significant number of events was the Tonga/Fiji region of the South Pacific, with 24 suitable earthquakes (Figure 6). In most other regions, only one or two events of $M_w \geq 5.5$ were present. These data are not included in this study.

Data

For each earthquake/station pair, the data were first rotated from the standard geographic N, E, Z (north/south, east/west, and vertical) reference frame into a ray coordinate reference frame of L, Q, and T components (Vinnik, 1977). As shown in Figure 7, in this reference frame, the L component corresponds to the apparent direction of P wave propagation. The Q component, which is orthogonal to L in the plane of propagation, corresponds to the direction of vibration for vertical S wave motion (SV). T is the transverse component, and all three components are mutually

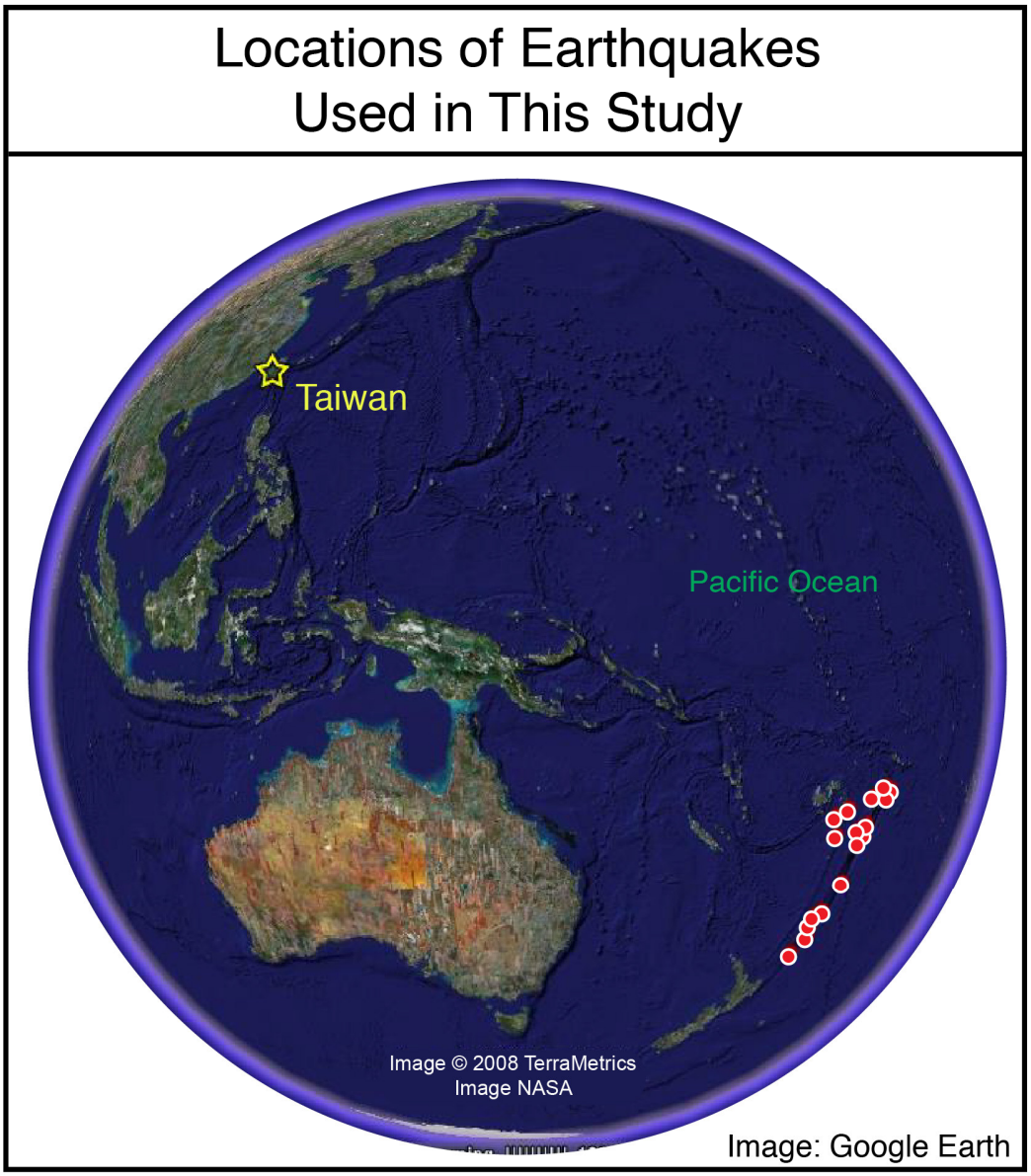

Figure 6. View of the western Pacific Ocean with selected seismic events. The island of Taiwan is marked with a yellow star, and the locations of the epicenters of earthquakes used in this study are marked with red circles.

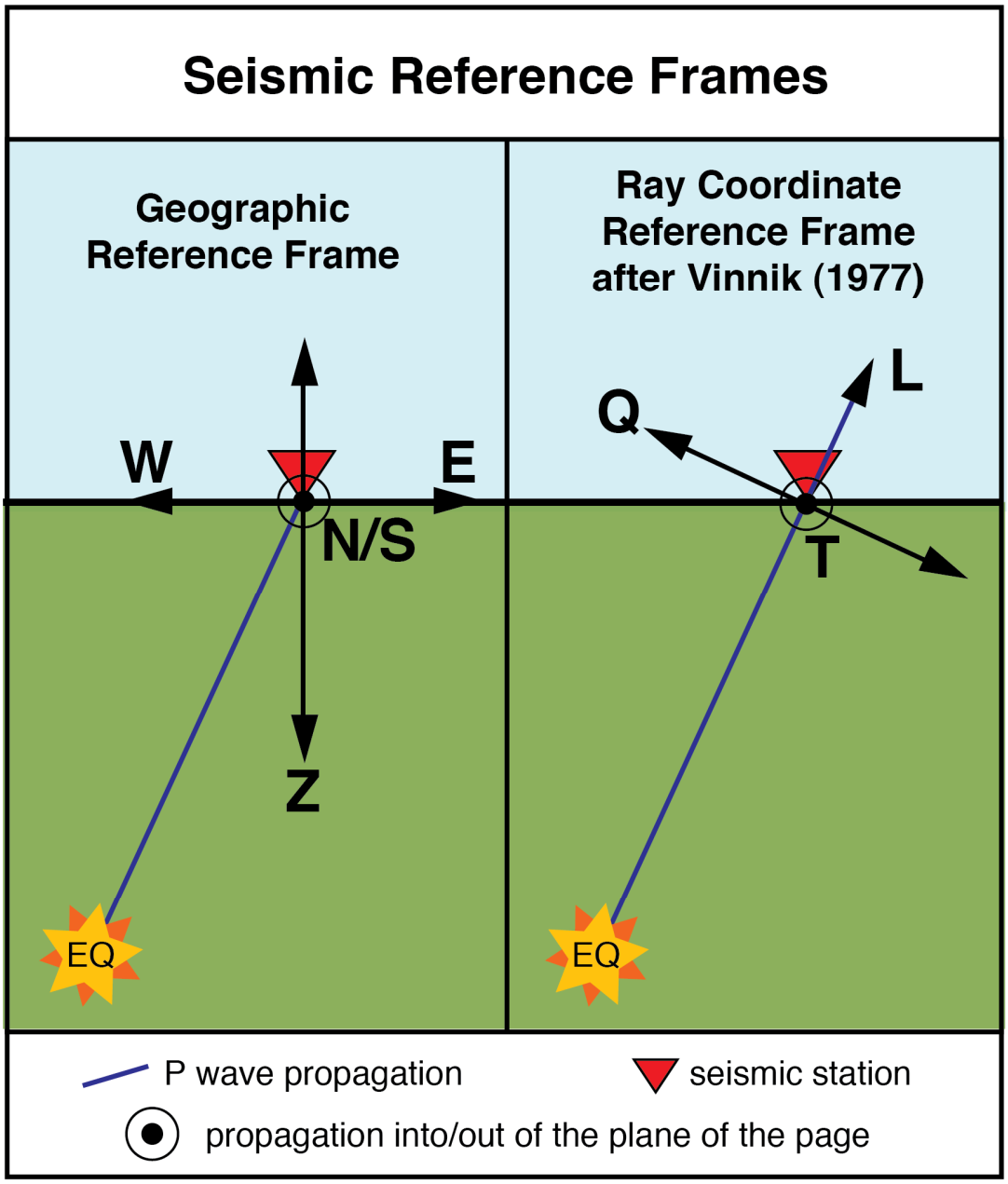
Seismic Reference Frames
Geographic Reference Frame
Ray Coordinate Reference Frame after Vinnik (1977)
W
E
N/S
Z
Q
L
T
EQ
EQ
P wave propagation
seismic station
propagation into/out of the plane of the page

Figure 7. Geographic Reference Frame vs. Ray Coordinate Reference Frame. On the left, the standard geographic reference frame used to record seismic energy is illustrated. Seismograms are oriented to record energy that propagates vertically (with respect to the surface of the Earth) and in two horizontal directions: north/south and east/west. On the right side of the figure, the Ray Coordinate Reference Frame, after Vinnik (1977) is illustrated. In this reference frame, seismic energy recorded in the standard geographic reference frame has been rotated using geospatial data from the seismic station and the earthquake focus to reorient the recorded seismic energy. The result is a three-component dataset where energy from P and S phases are isolated onto different components. The L component should present all of the P phase energy after rotation, and the Q component should present all of the SV phase energy.

perpendicular. By rotating the data into this reference frame, P and S phase energies are largely confined to a single component of the seismic record, making phase identification and receiver function analysis easier (Vinnik, 1977).

Prior to rotation, a 20 second high pass filter was applied to the data to remove any long period noise. In Figure 8 (a), 200 seconds of raw data from event C recorded at station TGC05 is shown. The main P arrival is plotted at the center of the figure, at 0 seconds. Figure 8 (b) presents the same data after initial filtering. All data manipulation, including phase rotation and the subsequent analyses, were carried out using the SeismicHandler software package (Stammler, 1993). In Figure 8 (c), the filtered data has been rotated into the ray coordinate reference frame. Back azimuths from observing stations to each earthquake were calculated using the TauP software package (Crotwell et al., 1999), and this information, along with the depth of the hypocenters, was used in the rotations. Figure 8 (d) presents the L and Q traces from the rotated data after a low pass filter (3 – 10 Hz) has been applied. A second example of rotated data from station TGC01 for event B is shown in Figure 9. Note the distinct P wave arrival on the L component and SV arrival on the Q component.

A spiking deconvolution centered on the primary phase of interest (in this instance, the P-wave) was then applied to the data to emphasize the signal, as shown in Figure 8 (e). In this process, the main P arrival was identified in the L component and the deconvolution time window of 90 seconds was set, with the P arrival time at the middle of the window. The deconvolution algorithm then identifies a similar wavelet in the Q component. A spike at the time of the P arrival is also inserted into the Q component for reference. Deconvolution also minimizes source function and propagation effects (Yuan et al., 2006). Data were then filtered using a low pass filter

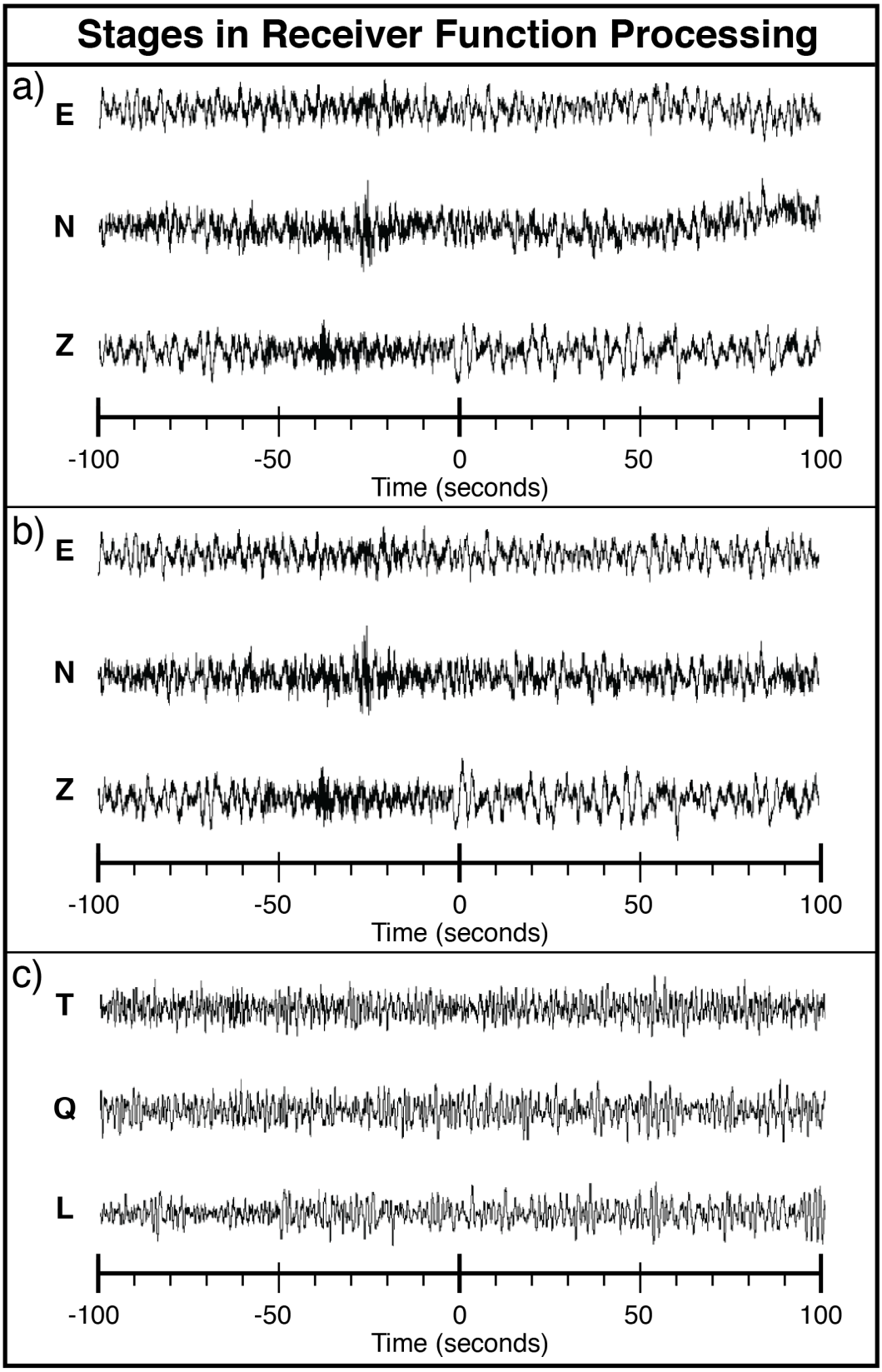
Stages in Receiver Function Processing
a)
E
N
Z
-100
-50
0
50
100
Time (seconds)
b)
E
N
Z
-100
-50
0
50
100
Time (seconds)
c)
T
Q
L
-100
-50
0
50
100
Time (seconds)

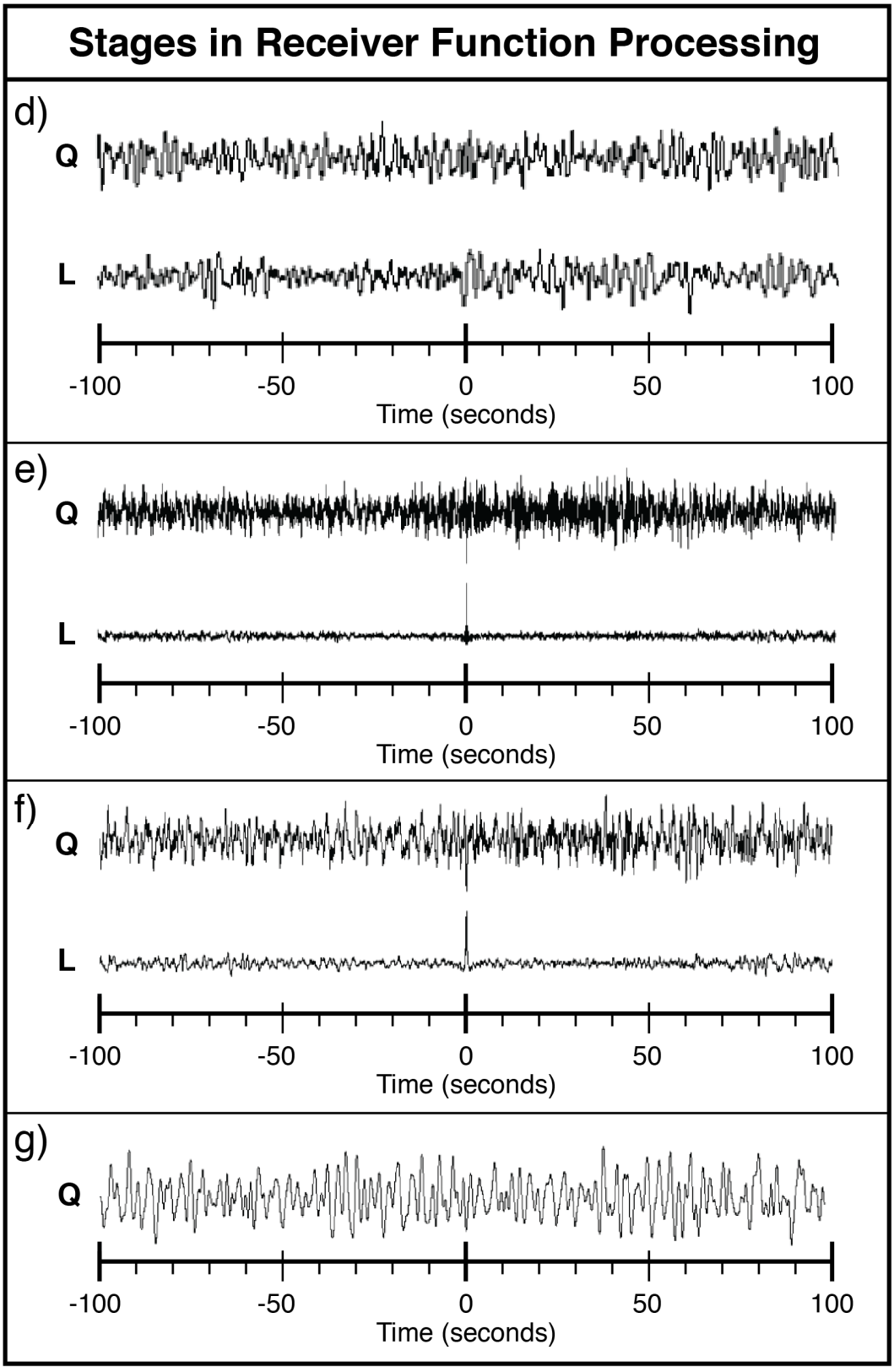
Stages in Receiver Function Processing
d)
Q
L
-100
-50
0
50
100
Time (seconds)
e)
Q
L
-100
-50
0
50
100
Time (seconds)
f)
Q
L
-100
-50
0
50
100
Time (seconds)
g)
Q
-100
-50
0
50
100
Time (seconds)

Figure 8. Example data illustrating the steps in receiver function processing from event C as recorded at station TGC05. (a) Raw data with the main P arrival (visible in the Z component) plotted at 0 seconds. Throughout this figure, the traces have been normalized to equal amplitudes. (b) Data after application of a 20 second high-pass filter. (c) Filtered data that has been rotated into the ray coordinate reference frame. Note that the P phase is now recorded primarily in the L component. (d) L and Q components from the high pass filtered, rotated data after a 3 Hz low pass filter has been applied. (e) L and Q components after spiking deconvolution to emphasize the converted Ps phase in the Q component. Note the strong spike in the Q component. The original P arrival in the L component is also emphasized by the deconvolution. (f) L and Q components after a second application of the 3 Hz low pass filter. (g) P wave receiver function for event C at station TGC05.

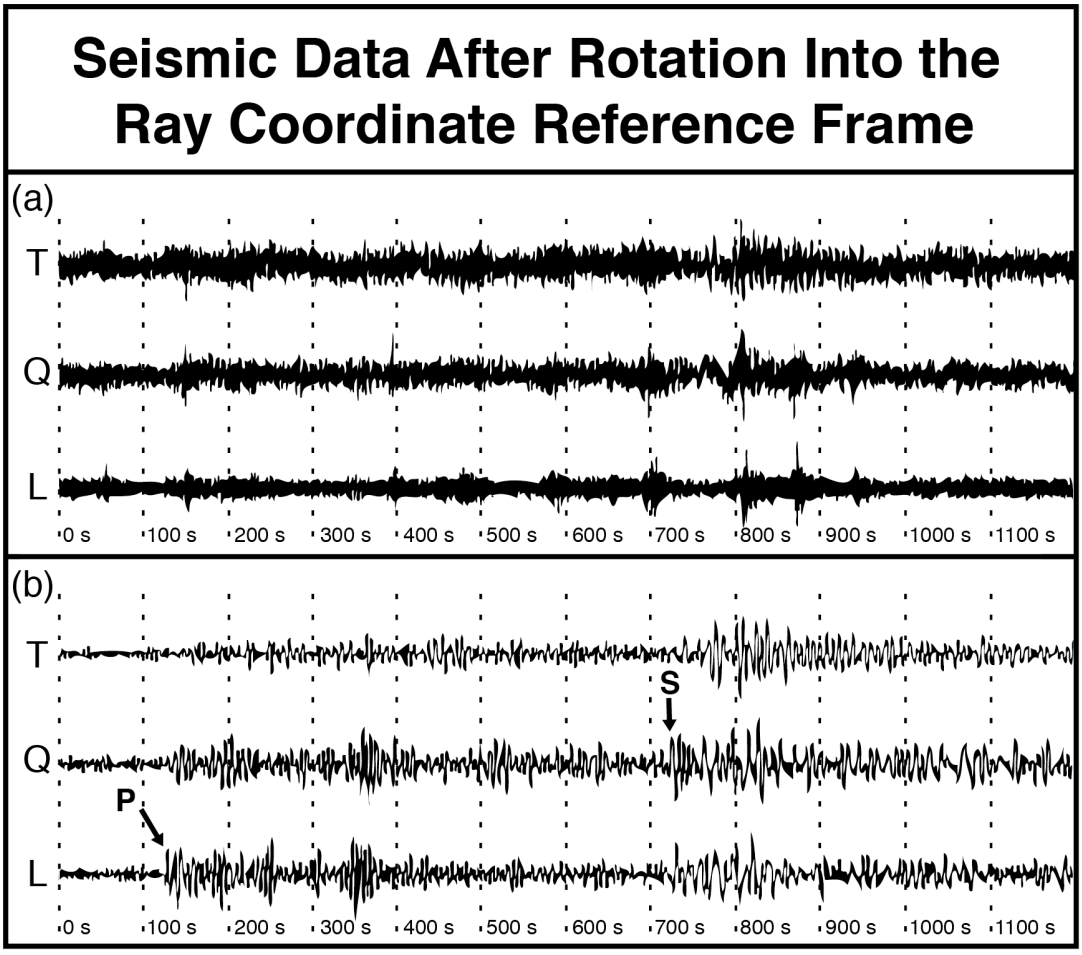

Figure 9. Example of seismic data after rotation into the Ray Coordinate Reference Frame. (a) Unfiltered L, Q, and T components of seismic data from event B (28 Sept. 2006, $M_O = 5.9$) for station TGC 01. (b) The same dataset after applying a low pass filter at 3 Hz. The main P and S arrivals have been marked.

at 3 - 10Hz (Figure 8 (f)) and individual components (L for PRFs and Q for SRFs) were inspected for a clear arrival, as described in the next paragraph. Finally, the events at each station were stacked in order to enhance the receiver function signal.

Prior to performing the receiver function analyses, filtered data were inspected for clear P and S arrivals. A handful of records that did not show clear arrivals were omitted from the study pool, as low-quality raw data did not yield usable receiver functions. Individual event receiver functions (i.e. Figure 8 (g)) were also examined prior to summing the traces. A handful of traces with excessive noise levels or those that were significantly discrepant from the majority were excluded from the stacks. For example, individual stations sometimes recorded unique signals that either did not contain the expected P and S arrivals, or that contained P and S arrivals that were very close together. Such discrepant records likely represent local human activities (mining, construction, etc.) or small local earthquakes not suitable for receiver function analyses, respectively. Inclusion of these events will unnecessarily obscure the signal in the stacked receiver function, as they did not contain the expected teleseismic data, and the amplitudes of these signals are often much greater than those of the converted phases used for receiver functions.

The earthquakes selected for use in this study were located in the Tonga-Fiji region at similar angular distances from stations though the hypocenters were at varied depths. The piercing points for the P and S waves for these events were tightly clustered with respect to the TAIGER stations. The average of the calculated piercing points at 35 km and at 210 km depth for P and S phases are plotted in Figure 10 (a-c). The tight clustering of each station's piercing points, within a 10 km radius, allows for stacking of individual receiver functions at a given stations. Individual receiver functions at each station are aligned using the main P or S phase arrival as appropriate and then summed to improve the signal to noise ratio.

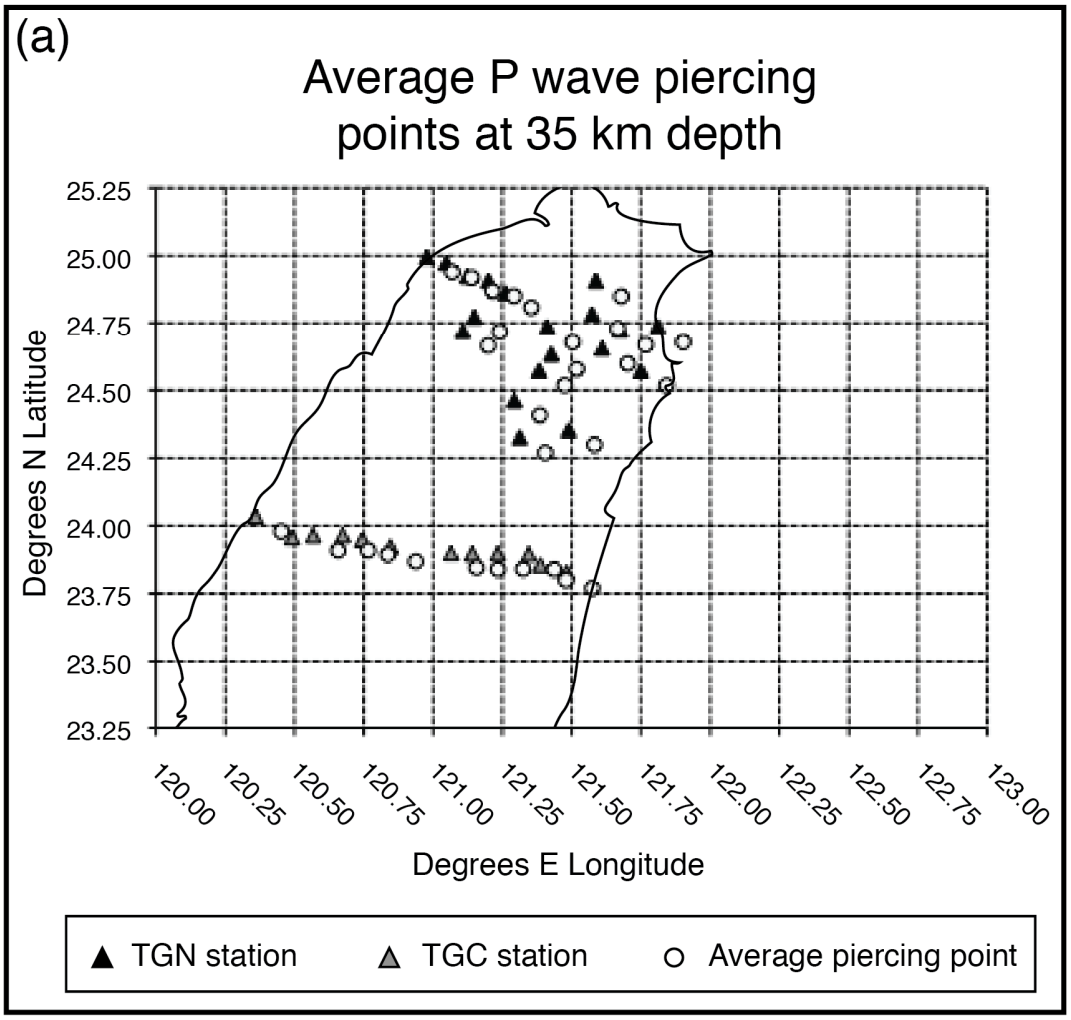
(a)
Average P wave piercing points at 35 km depth
Degrees N Latitude
25.25
25.00
24.75
24.50
24.25
24.00
23.75
23.50
23.25
120.00
120.25
120.50
120.75
121.00
121.25
121.50
121.75
122.00
122.25
122.50
122.75
123.00
Degrees E Longitude
TGN station
TGC station
Average piercing point

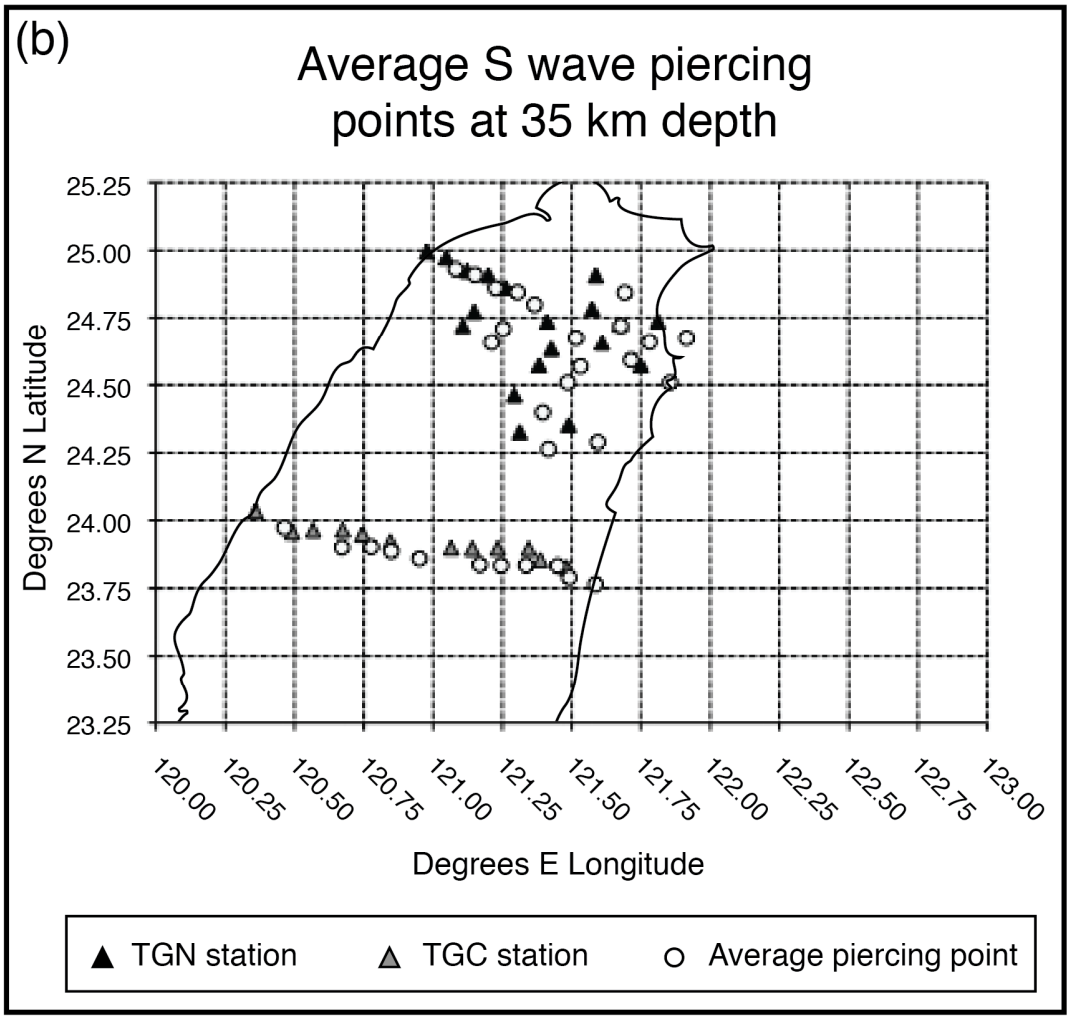
(b)
Average S wave piercing points at 35 km depth
Degrees N Latitude
25.25
25.00
24.75
24.50
24.25
24.00
23.75
23.50
23.25
120.00
120.25
120.50
120.75
121.00
121.25
121.50
121.75
122.00
122.25
122.50
122.75
123.00
Degrees E Longitude
TGN station
TGC station
Average piercing point

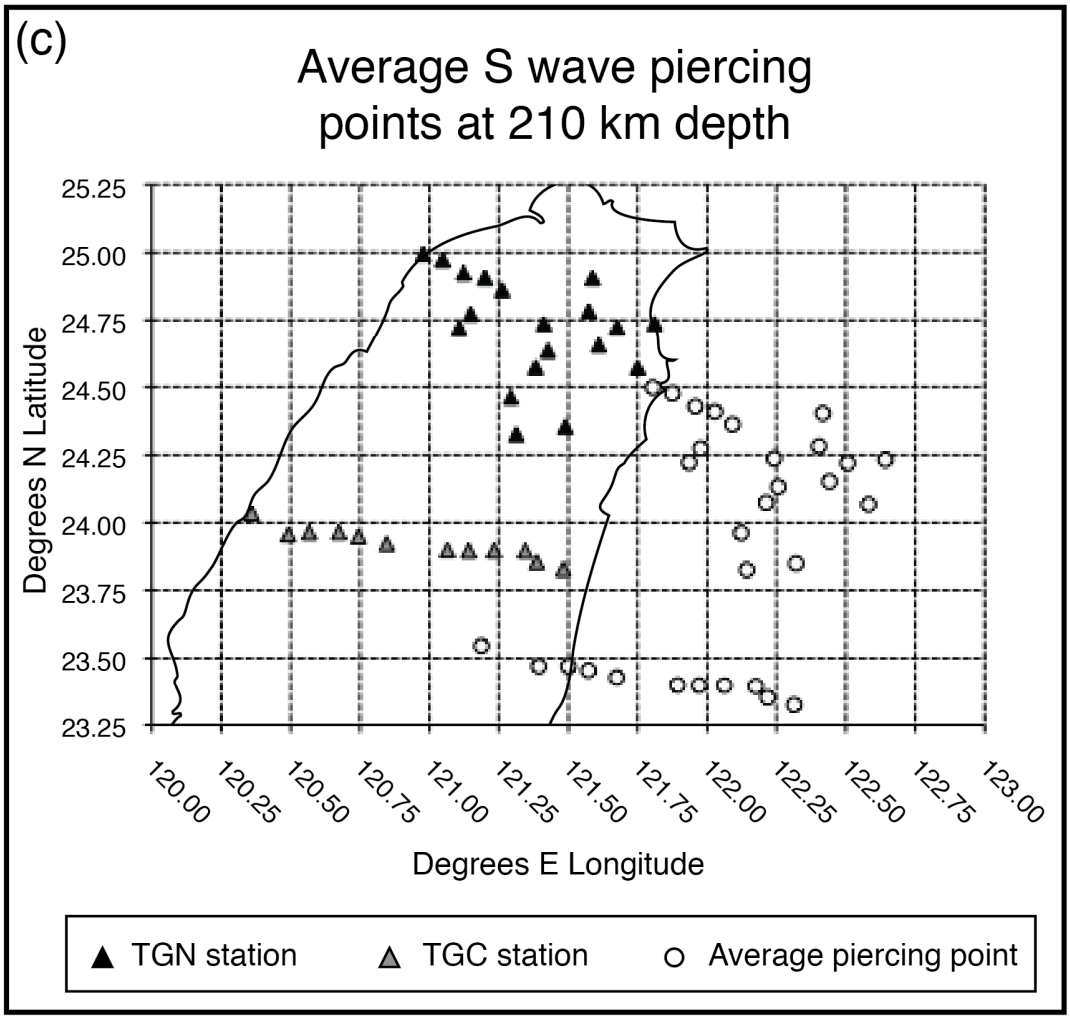

Figure 10. Average piercing points for the TAIGER stations. (a) Map of average P wave piercing points for each TAIGER station at 35 km depth. (b) Map of average S wave piercing points for each TAIGER station at 35 km depth. (c) Map of average S wave piercing points for each TAIGER station at 210 km depth. Because estimates of LAB thickness are performed only using SRFs, P wave piercing points at 210 km are not included.

The piercing points at 35 km depth, an estimated average depth at the base of the crust, plot approximately five to ten kilometers to the southeast of the seismic stations for both the P and S phases due to the fact that the up-going seismic rays are not perfectly vertical. P waves arrive at incidence angles between 15° and 22°, and S waves arrive at incidence angles between 18° and 25°. Consequently, the receiver functions provide information on the thickness of the crust just southeast of the seismic stations for Moho depths. For deeper targets, such as the base of the lithosphere, the piercing points are even further southeast of the seismic stations. For depths corresponding to the expected base of the lithosphere, piercing points for the seismic station-earthquake pairs used in this study could be 50 to 100 km southeast of the stations, or further. LAB depth estimates from this study are consequently plotted directly above the piercing points and not at the station coordinates.

In Figure 11, individual P wave receiver functions for station TGC07 are plotted together with a stacked trace. The P wave used to align the individual traces is plotted at zero seconds in the figure. Even though the P wave is identifiable in each individual trace, it is often difficult to pick out the converted Ps phase on the receiver function for a given earthquake, hence stacking to enhance the converted phases. In Figure 12, the individual S wave receiver functions and the stacked receiver functions for station TGC07 are shown. Again, the converted Ps phases are sometimes difficult to identify on the individual traces but are more easily observed in the stack.

Additional details of the receiver function processing protocol are included in the Appendix.

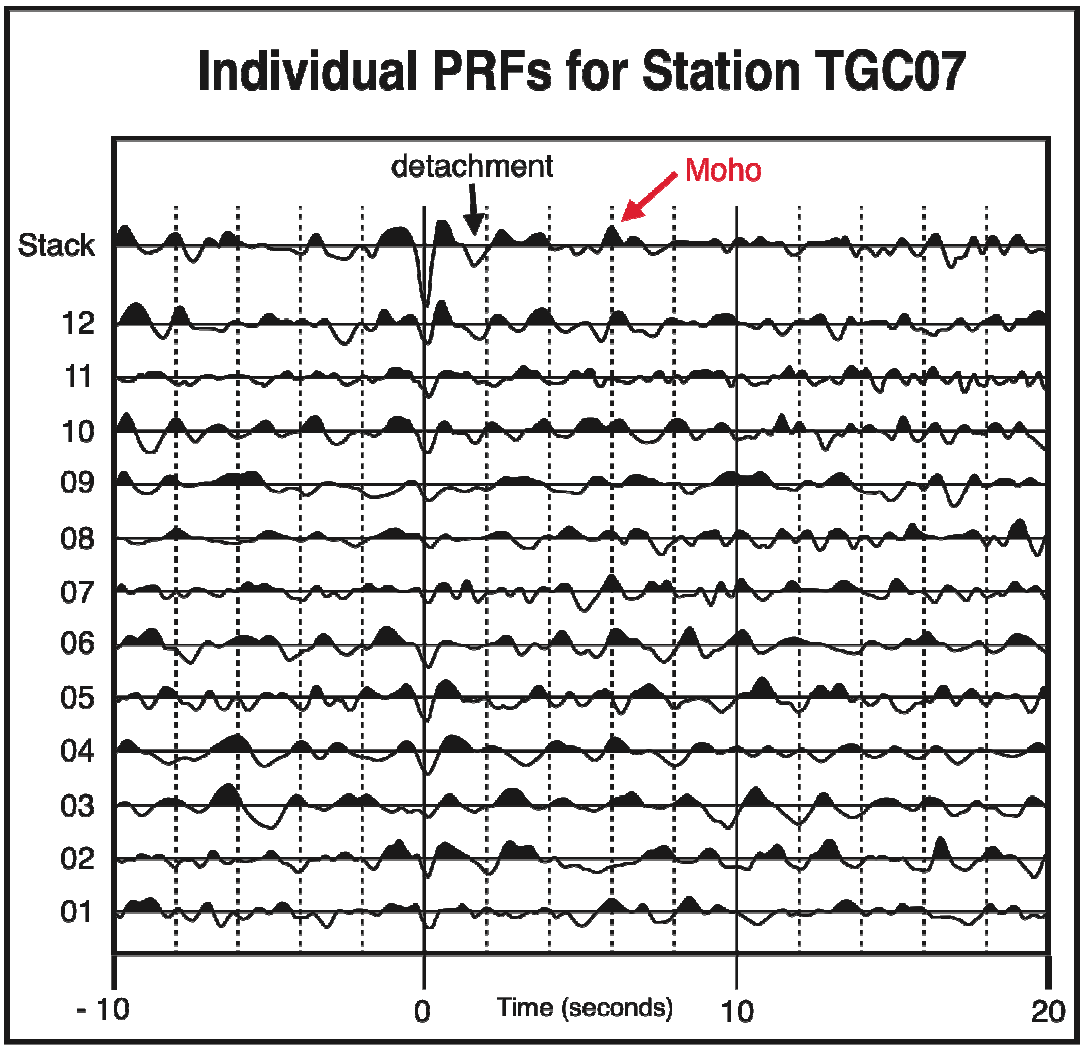

Figure 11. P wave receiver functions of 12 individual earthquakes for station TGC07. All traces are plotted with the P wave arrival at the zero time position. The converted Ps phase arrives shortly after the P wave due to the slower velocity after phase conversion. A distinct Ps arrival is not clear on many of the individual traces, however, the stack of each of the individual receiver functions plotted at the top of the figure does show a more coherent Ps phase at roughly 6 seconds. Amplitudes have been normalized for all traces, including the stack.

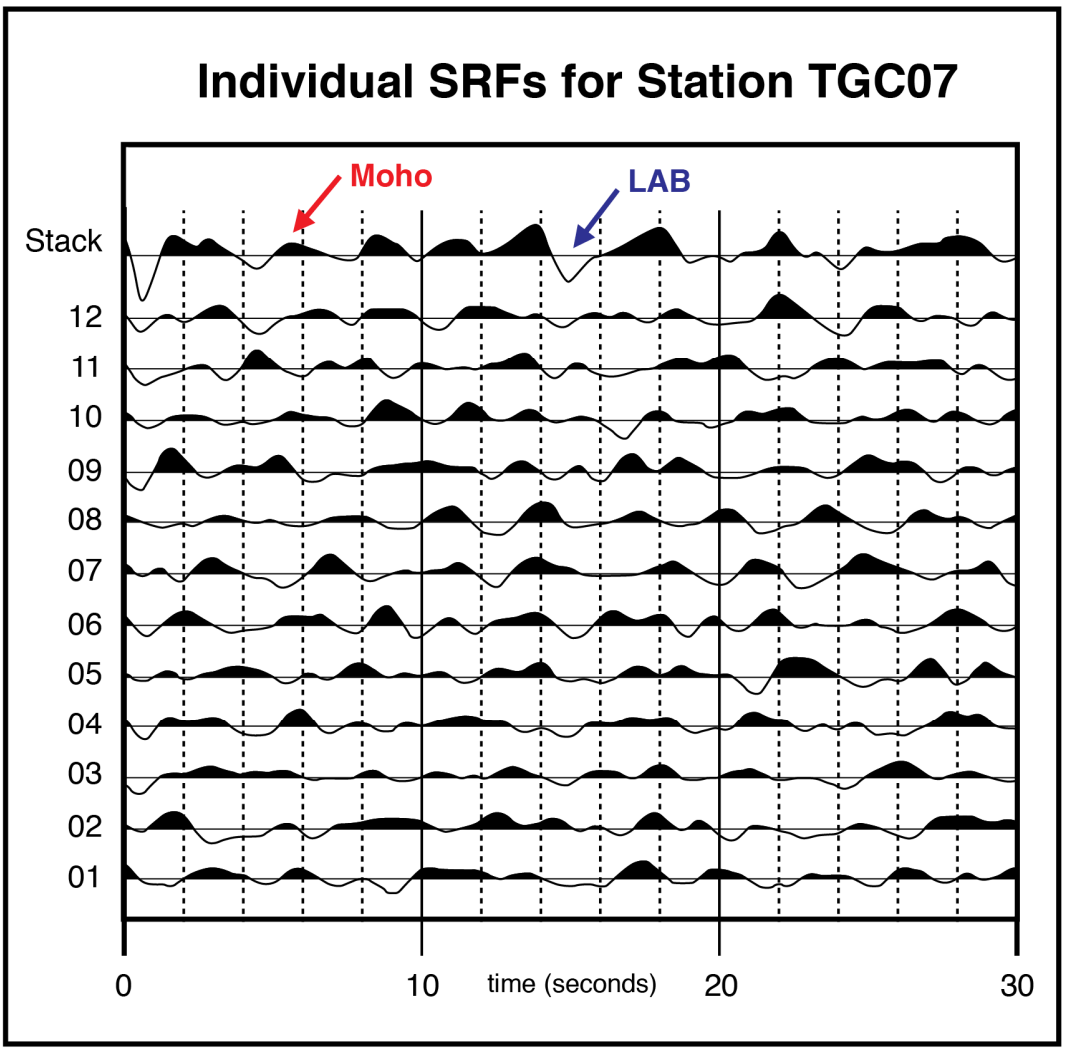

Figure 12. S wave receiver functions of 12 individual earthquakes for station TGC07. All traces are plotted with the S wave arrival at the zero time position. The time axis has been flipped during processing so that converted Sp phase will arrive shortly after the main S wave phase, allowing for direct comparison with the P wave receiver functions. Again, a distinct Sp arrival is not clear on many of the individual traces but a more coherent Sp phase is visible on the stack at roughly 6 seconds. Amplitudes have been normalized for all traces, including the stack.

MOHO TOPOGRAHY AND CRUSTAL FEATURES FROM RECEIVER FUNCTIONS

Interpretation of Receiver Functions

After processing and stacking, P wave receiver functions are inspected for signals from the Moho and any crustal converters while S wave receiver functions are inspected for signals representing waves converted at the Moho and the LAB. The arrival of the parent phase, either P or S, is considered to be time zero and converted rays will be recorded in the first few seconds following the parent arrival for PRFs and before the parent phase for SRFs. For ease of comparison with PRFs, the time scales on all SRFs in this study have been reversed so that converted phases appear after the parent phase and the polarities have been switched to be consistent with PRFs.

At the Moho, material with a lower seismic impedance lies on top of material with a higher seismic impedance. This results in a positive impedance contrast looking downward and we expect a positive amplitude feature in the receiver function. In contrast, a décollement in the crust would be expected to correspond to a negative impedance contrast as rock from depth, which is presumably denser than rock up-section, is thrust over lower density rock closer to the surface. At the LAB, higher impedance material lies on top of lower impedance material and the resulting impedance contrast is negative. As a result, the LAB will appear as a negative amplitude feature in receiver functions.

In the PRF stack at the top of Figure 11, a negative amplitude feature at approximately 2.0 seconds closely follows the P arrival (time zero). Corresponding to an estimated depth of ~17 km, this feature is too shallow to represent a conversion from the Moho beneath the Central Ranges and is instead interpreted as an eastward extension of the décollement fault seen in the Western Foothills. Similar features

appear in the stacked P wave receiver functions of several other western stations in the TGC group, including TGC03, 04, 06, and 08 (see Figure 13). The next significant positive amplitude feature in the receiver function stack for station TGC07 in Figure 11 occurs at approximately 6.0s and corresponds to an estimated depth of 50 km. This feature is interpreted as the Moho as it is the most prominent positive amplitude feature in this part of the receiver function. This Moho depth value also agrees well with Moho estimates from other sources (e.g. Kuo-Chen et al., 2010; Wu et al., 2004).

In Figure 12, the top-most trace is a stack of the 12 individual S wave receiver functions plotted below it. As with the PRFs in Figure 11, time zero represents the arrival time of the parent phase (in this case, the S wave). We again look for the first significant positive amplitude feature following time zero. In Figure 12, there are positive amplitude features at ~1.9 s and ~5.3 s, which correspond to estimated depths of ~15 km and ~40 km, respectively. In this instance, the deeper of the two is interpreted as a conversion from the Moho. Note that the P wave receiver function gave an estimated Moho depth of ~50 km for this station. However, given estimated errors of 6 to 10 km and 10 to 15 km for PRFs and SRFs respectively (Heit et al., 2008), these values are not considered significantly discrepant.

S wave receiver functions may also identify conversions from deeper impedance discontinuities, including the lithosphere-asthenosphere boundary, though these features are often more difficult to identify as the conversions are often convolved with the P wave coda. To identify possible LAB conversions in the SRFs, we look for significant negative amplitude features occurring later in the wavetrain than the Moho signals. In Figure 12, a distinctive negative amplitude feature occurs at ~15 s, indicating an LAB depth of ~144 km. In some receiver function stacks, there are multiple negative amplitude features that could represent conversions at the LAB.

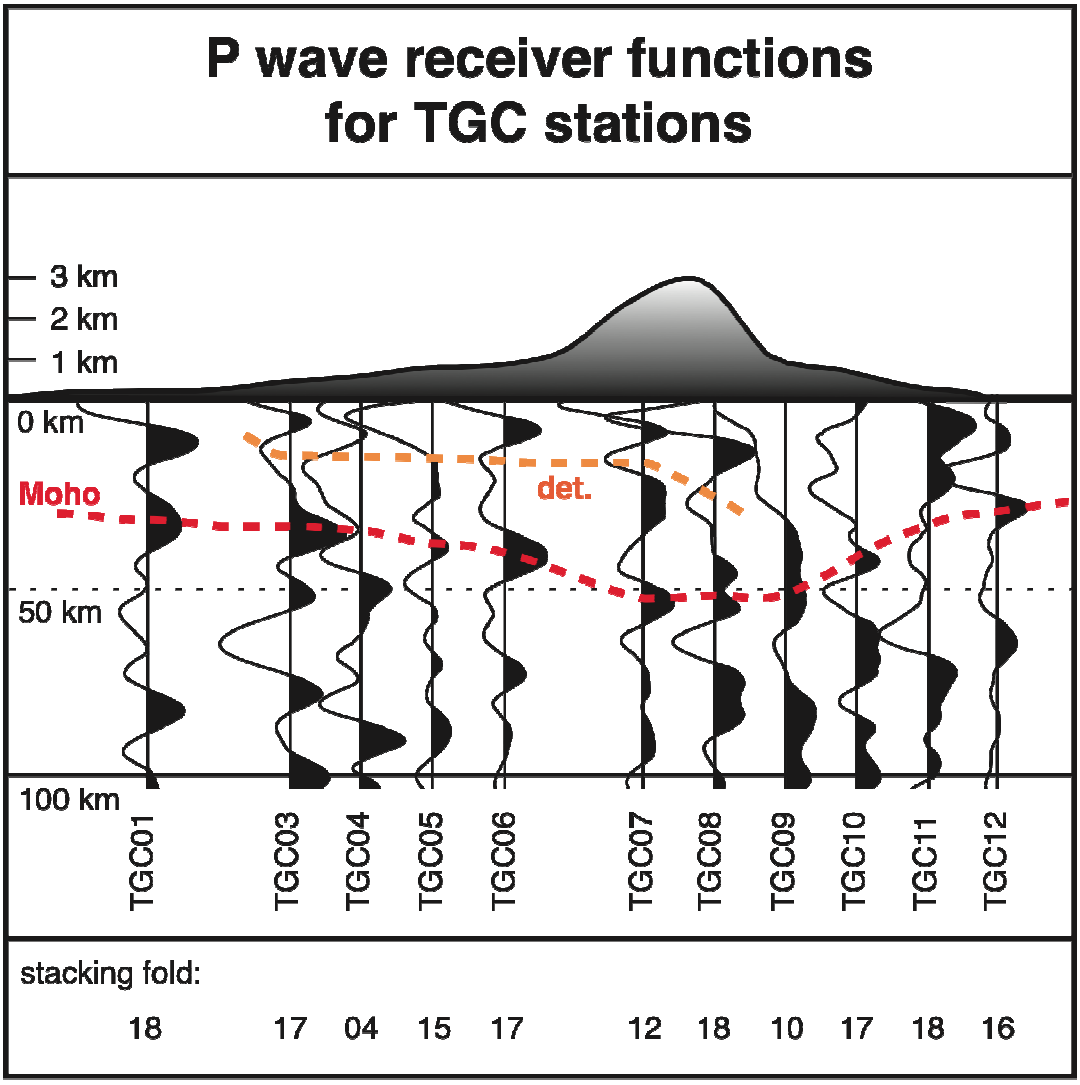

Figure 13. P wave receiver function stacks for the central group stations. Receiver functions from each individual earthquake have been stacked and plotted above the calculated 35 km piercing point for each station. The estimated depth to the Moho is marked with a dashed red line. The dashed orange line indicates the depth to the décollement under eastern central Taiwan. The stacking fold (the number of events used at each station) is given along the bottom of the diagram. The amplitudes of the stacks have been normalized as signal strength varies from station to station.

In these instances, time-to-depth conversions are calculated for each arrival and compared to other estimated values for the base of the lithosphere, and the feature with the best agreement is selected.

Central Group

The stations of the central group constitute a NW-SE trending transect across the island (Figure 4). Of the twelve stations, only station TGC02 was not included in the study as scarcity of its records and the high noise levels on the recorded events resulted in very poor quality data. The remaining eleven stations vary in their noise levels and in the number of events recorded, but all recorded data of sufficient quality and quantity for useful analysis. P wave receiver function results from the central group are presented in Figure 13 and 14 and the S wave receiver function results are presented in Figure 15 and 16. The Moho depth estimates for the central and northern stations are also given in Table 2.

In general, the stations located on the Coastal Plain and in the Western Foothills were generally more accessible and were consequently serviced more regularly, providing a more complete dataset. These locations, however, are also among the noisiest sites due to high levels of human activity in the region, reducing the data quality. The stations located in the Hsueshan and Central Ranges were more isolated, meaning noise levels were lower. As these stations were more difficult to access, they were serviced less regularly and fewer earthquakes were recorded as compared to the western stations. Stations located on the eastern side of the Central Ranges, in the Longitudinal Valley, or in Coastal Range were also subject to relatively low noise levels, but like those in the Central Ranges, these stations were sometimes difficult to access and data recovery was not consistent.

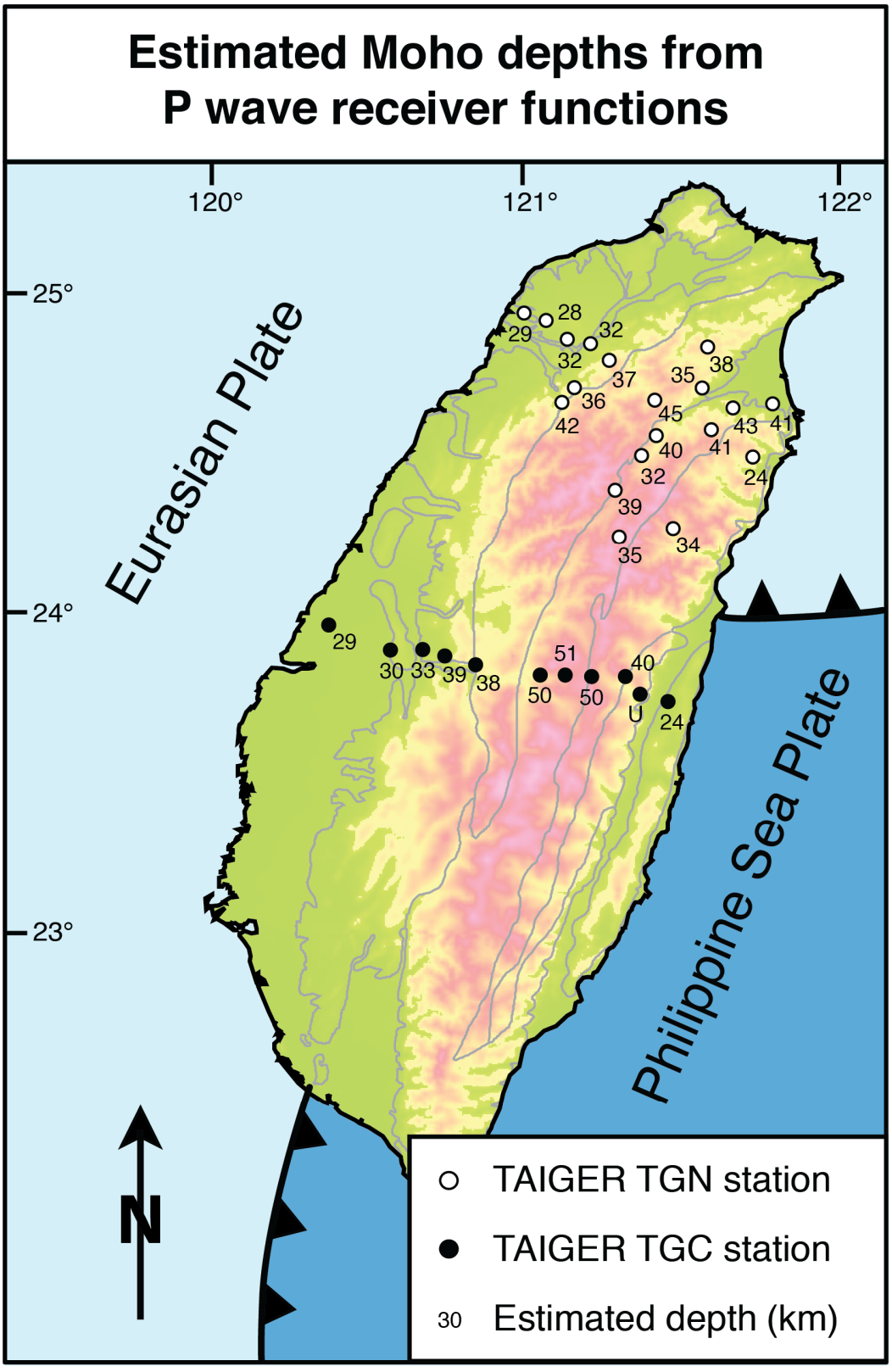
Estimated Moho depths from
P wave receiver functions
120°
121°
122°
25°
24°
23°
Eurasian Plate
Philippine Sea Plate
28
29
32
32
37
38
35
36
45
42
43
41
40
41
32
24
39
34
35
29
30
33
39
38
51
50
50
40
U
24
N
TAIGER TGN station
TAIGER TGC station
30 Estimated depth (km)

Figure 14. Map of estimated Moho depths from P wave receiver functions for the northern and central groups. The numbers plotted next to each station indicate the estimated Moho depth. "U" indicates a station where P wave receiver functions did not show a clear Moho signal and no depth estimate was made. In most instances, the numbers are plotted approximately 10 km to the southwest of each station, above the calculated 35 km depth piercing points, except for stations TGC08 and TGC 10, where the depth estimates have been plotted north of the stations for the sake of legibility.

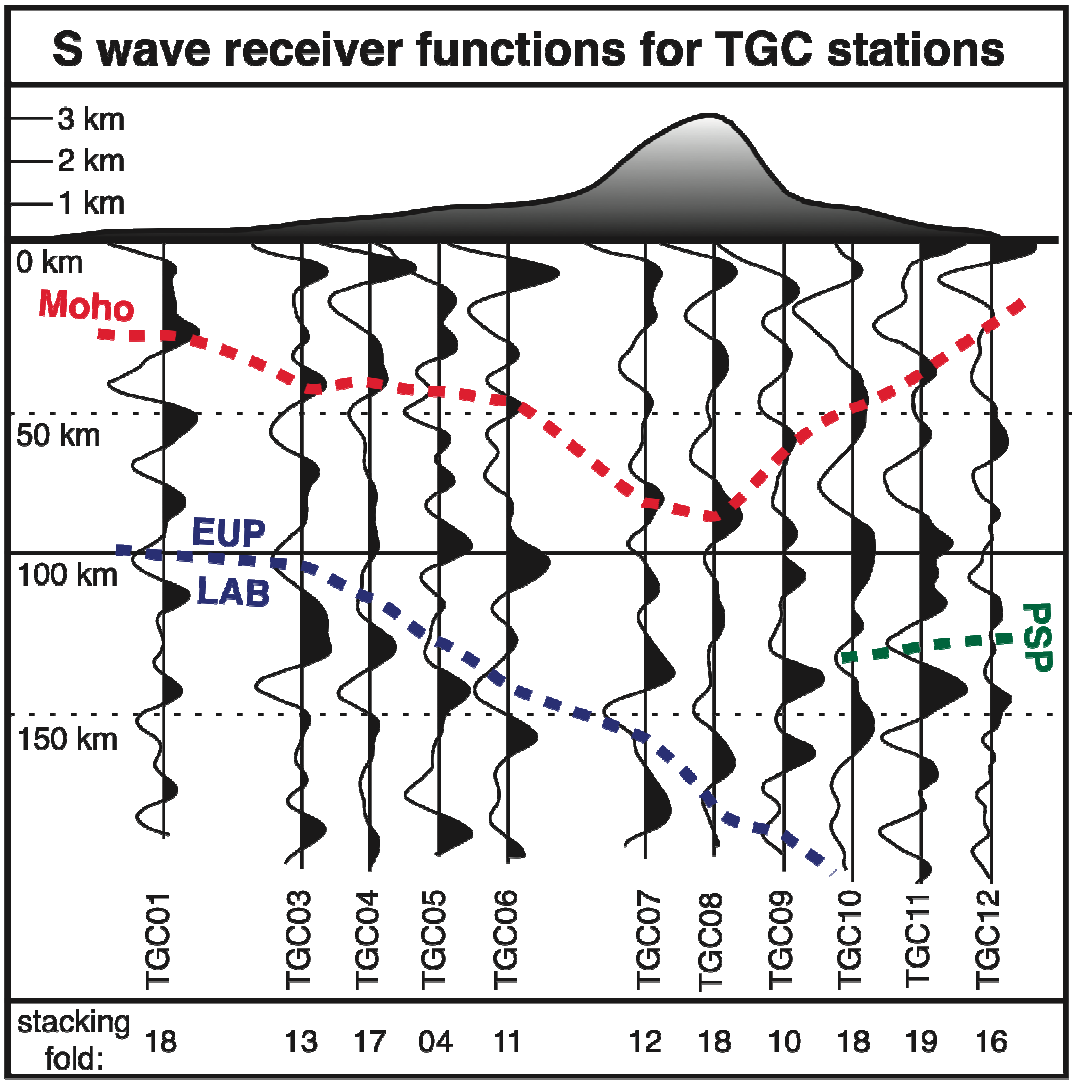

Figure 15. S wave receiver function stacks for the central group stations. Receiver functions from each individual earthquake have been stacked and plotted above the piercing point for each station. The estimated depth to the Moho is marked with a dashed red line. The estimated depth of the Lithosphere-Asthenosphere Boundary (LAB) for the Eurasian Plate (EUP) is marked with a dashed blue line. The possible depth of the LAB for the Philippine Sea Plate (PSP) is marked with a dashed green line on the right side of the figure. Stacking and normalization as in Figure 9.

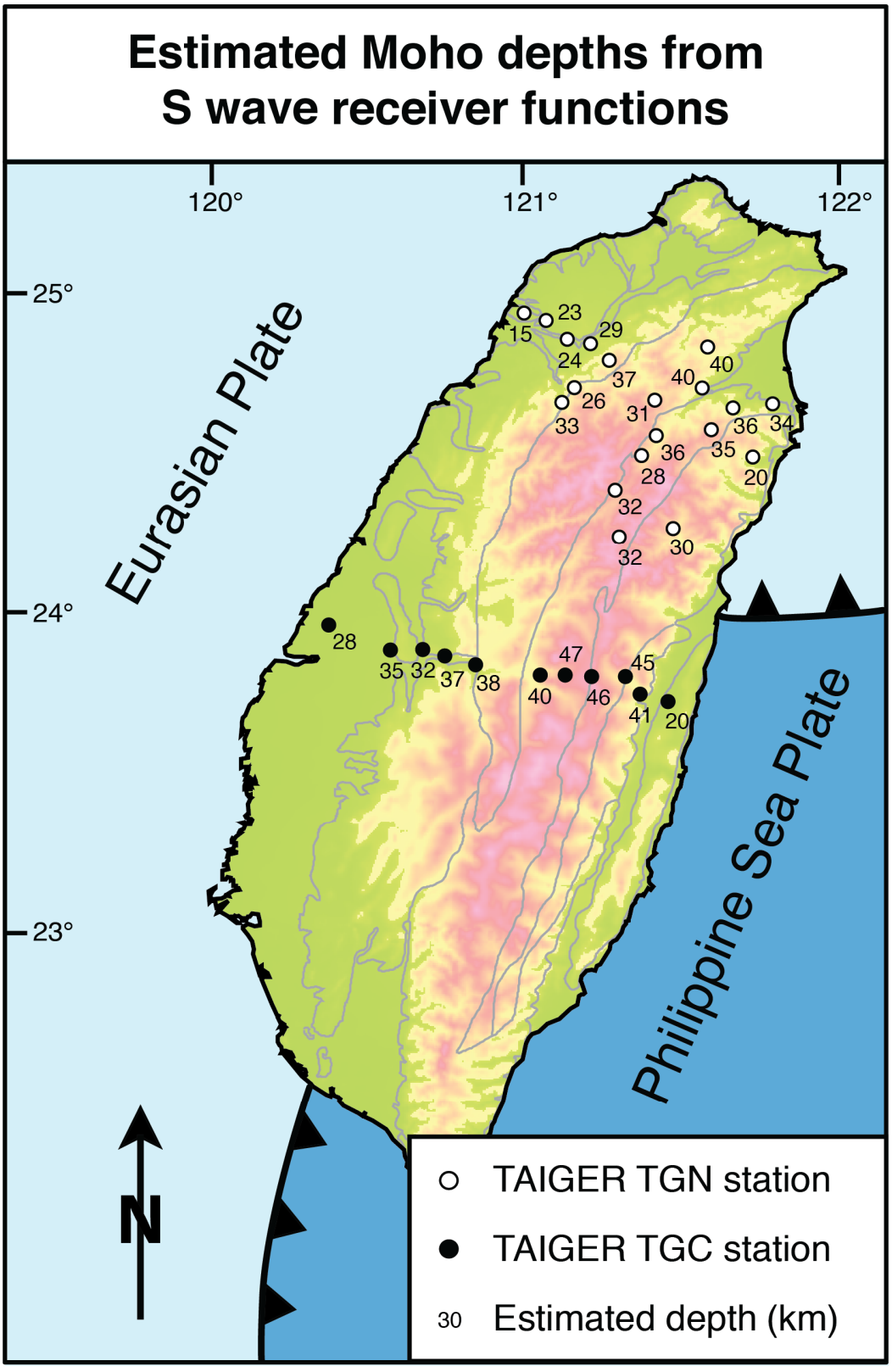
Estimated Moho depths from
S wave receiver functions
120°
121°
122°
25°
24°
23°
Eurasian Plate
Philippine Sea Plate
15
23
29
24
37
40
40
26
31
33
36
34
35
36
20
28
32
32
30
28
35
32
37
38
47
40
46
45
41
20
N
TAIGER TGN station
TAIGER TGC station
30 Estimated depth (km)

Figure 16. Map of estimated Moho depths from S wave receiver functions for the northern and central groups. The numbers plotted next to each station indicate the estimated Moho depth. In most instances, the numbers are plotted approximately 10 km to the southwest of each station, above the calculated 35 km depth piercing points, except for stations TGC08 and TGC 10, where the depth estimates have been plotted north of the stations for the sake of legibility.

Table 2. Moho depth estimates from P wave and S wave receiver functions for seismic stations in the central and northern TAIGER groups.

Station	PRF Moho Estimate (km)	SRF Moho Estimate (km)	Number of Events Used (PRF, SRF)
TGC01	29	28	19, 19
TGC03	30	35	17, 17
TGC04	33	32	2, 13
TGC05	39	37	11, 5
TGC06	38	38	17, 11
TGC07	50	40	12, 12
TGC08	51	47	8,6
TGC09	50	46	11, 11
TGC10	40	45	18, 19
TGC11	unclear	41	NA, 19
TGC12	24	21	16, 16
TGN01	29	16	13, 12
TGN02	28	23	13, 13
TGN03	32	24	14, 14
TGN04	32	29	13, 13
TGN05	37	37	3, 1
TGN06	45	31	5, 4
TGN08	41	35	1, 1
TGN09	24	20	15, 15
TGN11	38	40	5, 5
TGN12	35	40	15, 11
TGN13	43	36	16, 15
TGN14	41	34	14, 12
TGN15	42	33	3, 3
TGN16	35	26	10, 8
TGN17	40	36	14, 14
TGN18	32	28	16, 12
TGN19	39	32	12, 15
TGN20	35	32	10 19
TGN21	34	30	4, 13

As previously discussed, P wave receiver functions from several of the western and central stations in the TGC group display negative amplitude features at times earlier than would be expected for conversions from the base of the crust. These features are consequently interpreted as an intra-crustal feature, specifically a single décollement or a series of thrust faults above a basal décollement, which extend from the toe of the Western Foothills (TGC03 and TGC04), through the Hsueshan Range (TGC06), and into the Western Central Range (TGC07 and TGC08). The décollement is estimated at a depth of approximately 15 km in the west (TGC03), deepening to nearly 30 km in the Western Central Range, and extending approximately 18 km to the east of the Lishan Fault.

The PRF and SRF results indicate a Moho depth beneath the Eurasian plate of approximately 30 km for stations TGC01 and TGC03. Ai et al. (2007) estimated average Moho depths in the Fujian region of China at 31.1 km, indicating that the crust has not thinned significantly in western Taiwan. Moving to the east, the Moho deepens to ~33 km at TGC04, ~38 km at TGC05 and TGC06. The SRF processing for the next three stations, TGC07, TGC08, and TGC09, does not yield a Moho signal that is as easily identifiable as in the PRF results. PRF results for stations TGC07 and TGC09 indicate a Moho depth of ~50 km, with a slightly deeper estimate of ~51 km beneath TGC08. PRF and SRF results indicate a Moho depth of ~43 km at TGC10. PRF results are inconclusive at TGC11, though the SRF analysis suggests a Moho depth of ~41 km. At station TGC12, PRF and SRF results indicate Moho at ~23 km. The inconsistencies between the PRF and SRF Moho estimates may be due to the fact that a single velocity model was used for all of the stations, neglecting possible lateral velocity variation from region to region. Additionally, a tomographic study done by Wu et al. (2007) indicates an anomalous zone of low Vp / Vs beneath the Central

Ranges. This low ratio may explain why the SRF Moho estimates tend to yield shallower values than the PRF estimates for stations TGC07, TGC08, and TGC09, as discussed previously. If Vs values at crustal depths in the Central Ranges are higher than expected, the time to depth conversions for the SRF estimates will systematically under-predict the Moho depth. Such variations are discussed further in the next section.

The Moho morphology for the Central transect indicates a Moho depth of roughly 50 km beneath the central part of Taiwan, suggesting approximately 60% crustal thickening beneath the orogen when compared to the Moho depth of approximately 30 km, as estimated from station TGC01, where the crust is undeformed. This supports the inference that convergence between the Eurasian continental margin, with an initial thickness of ~30 km, as estimated from station TGC01 and receiver function studies of southeastern China by Ai et al. (2007), and the Philippine Sea oceanic crust, at ~23 km thick, has significantly thickened the crust. Collision and deformation have created a crustal root beneath the Central Ranges that extends to a depth of approximately 50 km.

Northern Group

The stations of the northern group follow a similar geographic pattern of noise levels and data preservation to that of the central group, with the stations closest to the western and eastern coasts of the island having both the highest noise levels and the highest data recovery. Stations located in more remote mountainous areas were generally less noisy but also suffered from non-uniform data recovery. Stations located along the Lanyang River valley southwest of the city of Ilan (see Figure 2) were also subject to high noise and were regularly serviced, with similar data quality and quantity to the coastal stations. Full PRF and SRF estimates of the Moho depth are

given in the lower portion of Table 2. The PRF curves for stations TGN01 through TGN09 are plotted in Figure 17 and the SRF curves for these stations are given in Figure 18. These data are also presented on the maps in Figures 14 and 16, respectively.

In the northern group, stations TGN01 through TGN06, TGN08, and TGN09 lie along a transect parallel to the central group stations and to the direction of convergence. From the PRF results, the Moho depth is estimated at ~29 km and ~28 km beneath stations TGN01 and TGN02, respectively. Moving to the east, the Moho deepens to ~32 km at TGN03 and TNG04, and ~37 km at TGN05. Both the PRF and SRF results for station TGN06 are inconclusive. As a group, the stations in the northern group suggest a thickened crust in the central part of the island, similar to results from the central group.

The Moho is estimated at ~41 km from P wave receiver functions beneath station TGN08, and at ~35 km from the S wave receiver functions. For station TGN09, the PRF results give an estimated Moho depth of ~24 km, while SRF results suggest a Moho depth of ~20 km. The discrepancies between the PRF and SRF Moho depth estimates for these two stations may be due to intrusion of partially molten material related to magmatic activity at the Ryukyu Arc as rifting at the Okinawa Trough propagates landward, as suggested in tomography by Kuo-Chen et al. (2010). Increased fluid content in the crust would likely decrease the Vs, which would yield shallower Moho depth estimates for the PRFs, resulting in better agreement between the SRF and PRF results. A modest decrease in average Vs from 3.93 km/s to 3.67 km/s (corresponding to an increase in the Vp / Vs ratio from 1.62 to 1.74 with constant Vp) would bring the two Moho estimates to within a kilometer of one another. Alternatively, the tear fault in the Eurasian Plate beneath northeastern Taiwan may cause teleseismic waves to deviate from the expected raypaths and consequently to

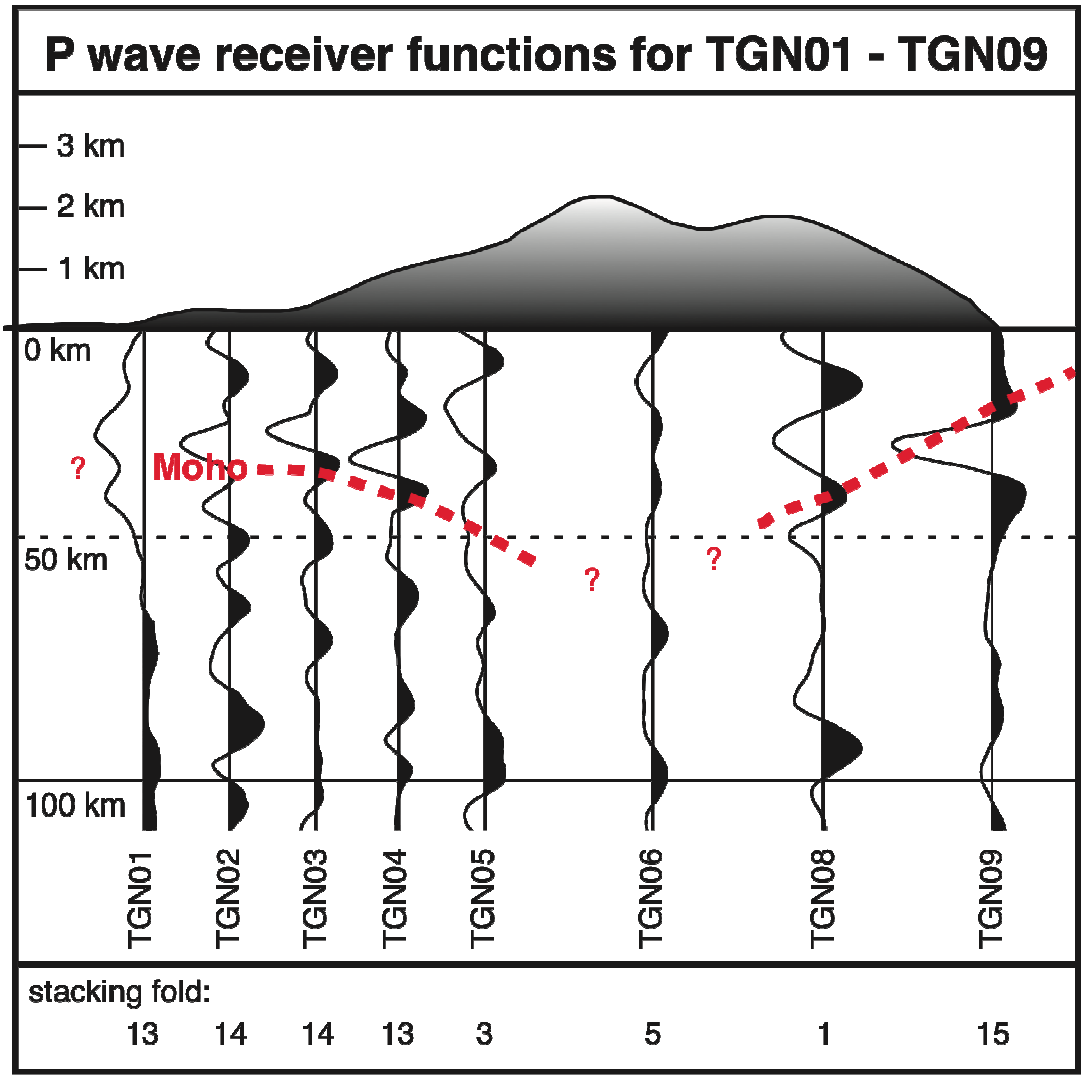

Figure 17. P wave receiver function stacks for the northern group stations TGN01 – TGN09. Receiver functions from each individual earthquake have been stacked and plotted above the calculated 35 km piercing point for each station. The estimated Moho conversions are marked with a dashed red line. A clear Moho conversion is not seen in the receiver functions for stations TGN01, TGN02, TGN05, and TGN06. In general, the stations in the northern group were noisier than those in the central group, making phase identification more difficult. Stacking and normalization as in Figure 10.

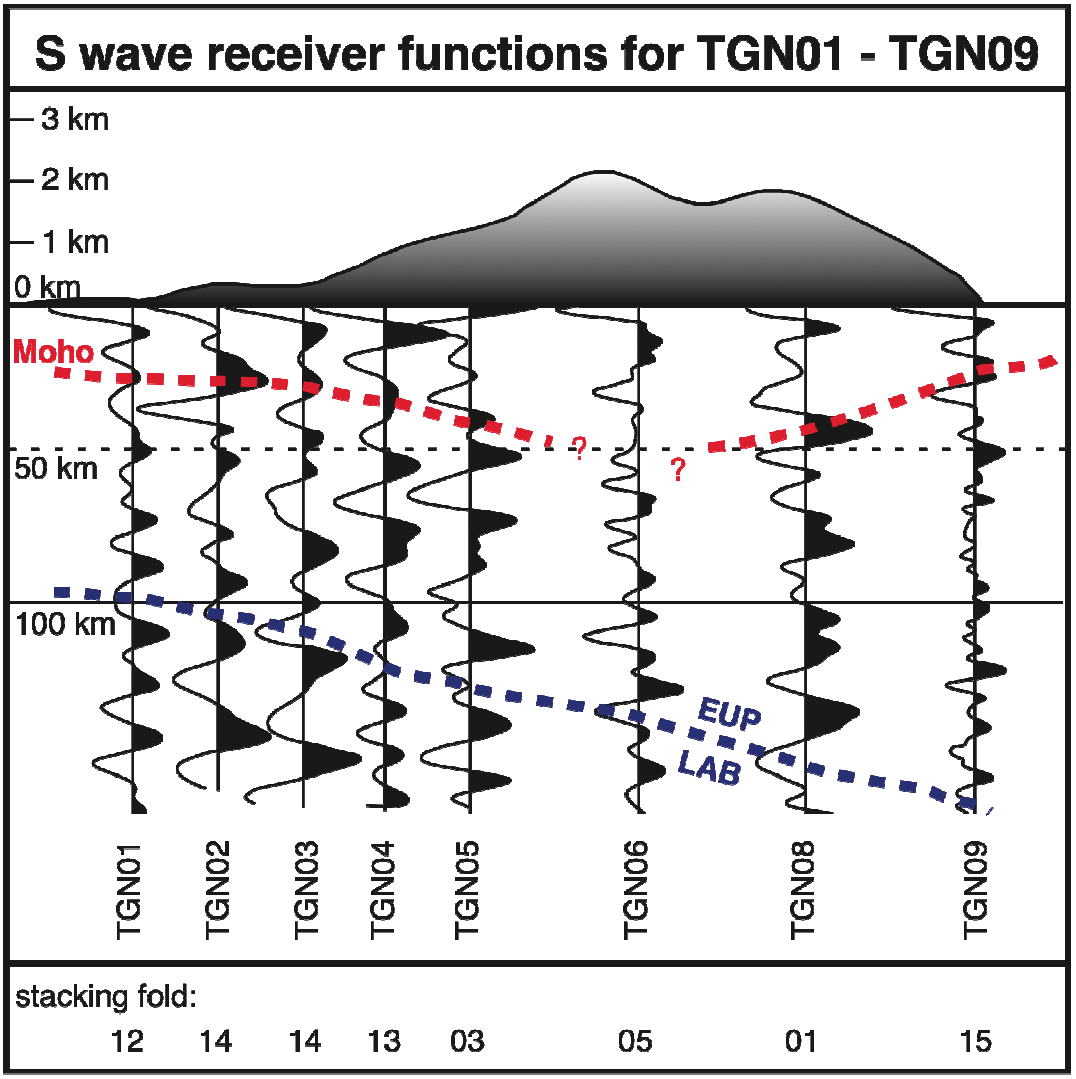

Figure 18. S wave receiver function stacks for the northern group stations TGN01 – TGN09. Receiver functions from each individual earthquake have been stacked and plotted above the calculated 35 km depth piercing point for each station to facilitate comparison with the PRF Moho depth estimates. The estimated Moho conversions are marked with a dashed red line. The estimated depth of the LAB for the Eurasian Plate (EUP) is marked with a dashed blue line. Stacking and normalization as in Figure 10.

sample different portions of the crust. This deviation and the resultant offset of piercing points may be the cause of the discrepancy between the PRF and SRF Moho estimates in the area surrounding stations TGN08 and TGN09, though it is likely that deviations from modeled velocity values contribute to the discrepancy at these stations as well.

P wave receiver function stacks from the remaining northern group stations are presented in Figure 19. S wave receiver function stack for these stations are presented in Figure 20. These stations will be described in several geographic sub-groupings in the following paragraphs.

Stations TGN05, TGN15, and TGN16 are located along a northeast/southwest trending line where the Western Foothills transition to the Hsueshan Range in northwestern Taiwan. PRF and SRF results for TGN05 indicate a Moho depth of ~37 km, but results for stations TGN15 and TGN16 are more variable. PRF results for TGN15 indicate a Moho depth of ~42 km while SRF results suggest a depth of ~33 km. For station TGN16, the PRF results give a Moho estimate of ~35 km and the SRF results put the Moho much shallower at ~26 km. Of these, the SRF Moho estimate for station TGN16 is the least robust (see Figures 19 & 20). Although the PRF and SRF results for station TGN15 vary by nearly 10km, these values are within the expected error of ~6 km for PRFs and ~10 km for SRFs (Heit et al., 2008). The remaining receiver functions give an average Moho depth of ~37 km for stations located along the transition from the Western Foothills to the Hsueshan Range, again within error of the seemingly discrepant values for TGN15. A Moho depth of ~37 km indicates a slight thickening of the continental margin crust has occurred at the edge of the mountain range and is consistent with Moho depth estimates from TGC04 and TGC05, which are similarly located where the Western Foothills transition to the Hsueshan Range.

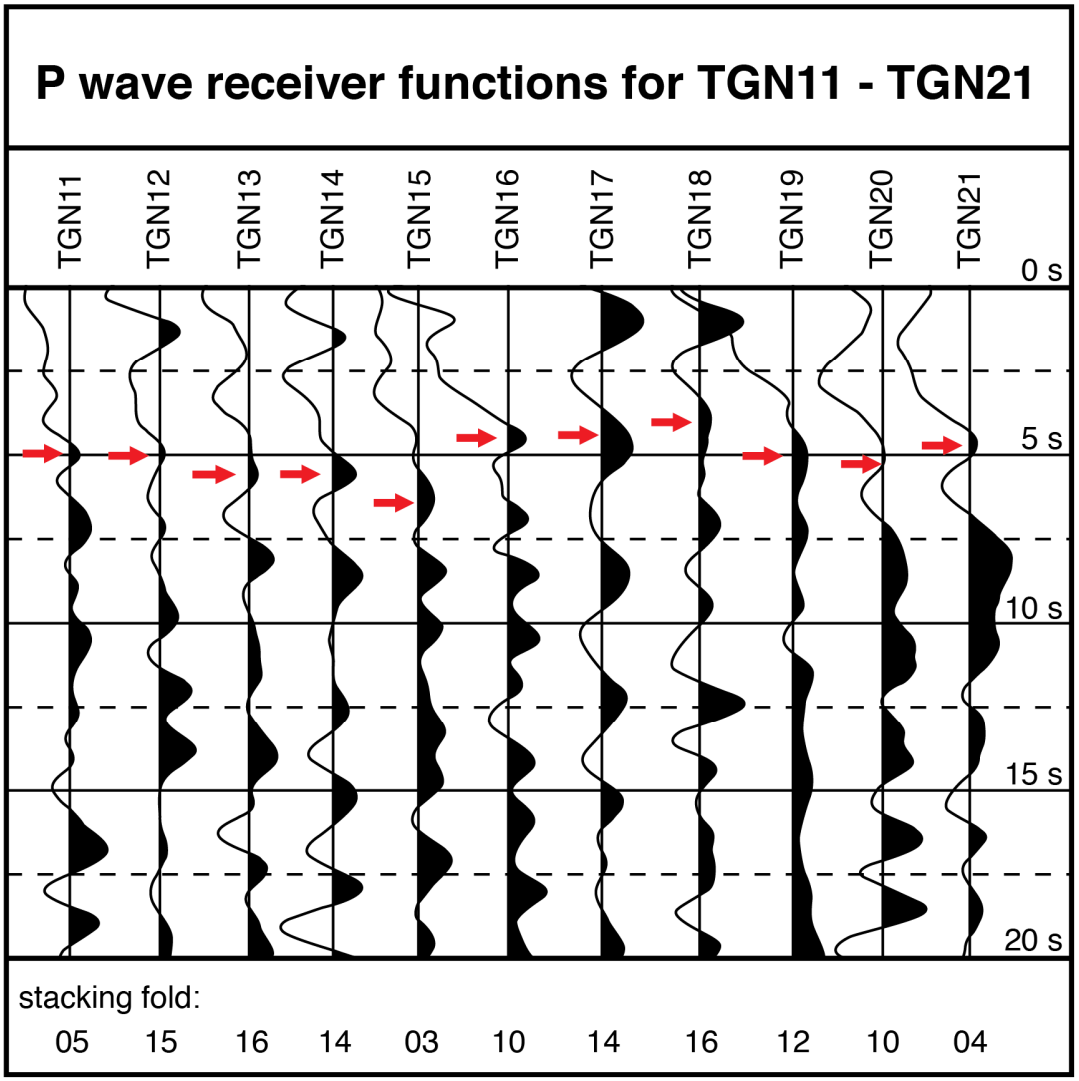

Figure 19. P wave receiver function stacks for the northern group stations TGN11 – TGN21. The estimated Moho conversion for each stack is indicated with a red arrow to the left of the curve. Receiver functions from each individual earthquake have been stacked and plotted for each station. Stacking and normalization as in Figure 10. These stations are generally much noisier than the stations in the central group and the Moho conversions are not very robust. Please note that these stations are do not lie along a single geographical transect of the island and the results should not be read as such.

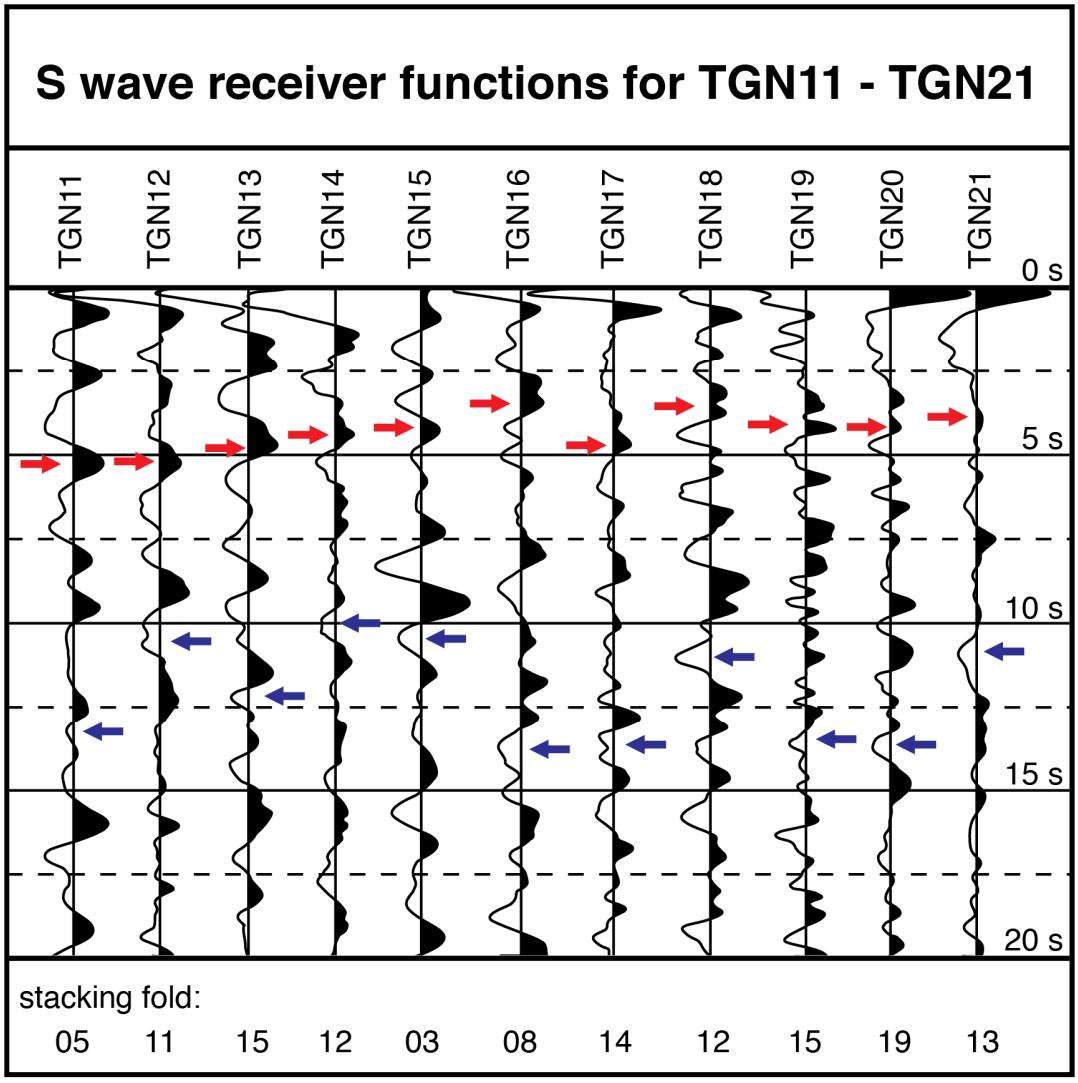

Figure 20. S wave receiver function stacks for the northern group stations TGN11 – TGN21. The estimated Moho conversion for a given station is indicated with a red arrow to the left of each curve. The estimated LAB conversion is indicated with a blue arrow to the right of each curve. Receiver functions from each individual earthquake have been stacked and plotted for each station. Stacking and normalization as in Figure 10. These stations are generally much noisier than the stations in the central group and the Moho conversions are not very robust. Please note that these stations are do not lie along a single geographical transect of the island and the results should not be read as such.

Stations TGN11 through TGN14 are located in and around the Ilan Plain in northeastern Taiwan, which represents the landward propagation of the Okinawa Trough (e.g. Hou et al., 2009), a complex and active region of the Taiwan orogen. PRF and SRF results indicate average Moho depths of ~39 km for station TGN11, of ~38 km for stations TGN12 and TGN14, and of ~40 km for station TGN13. These Moho depth values are shallower than those at the core of the orogen (between 46 km and 51 km at TGC08 and TGC09) and suggests that either: (a) crustal thickening has not been as extreme in the northern part of Taiwan, or (b) previously thickened crust has experienced more recent thinning due to the back-arc spreading at the Okinawa Trough.

Stations TGN17 through TGN19 are located along the Lanyang River Valley and the Lishan Fault. These stations show some variability in the estimates of Moho from receiver functions. TGN17, the furthest north of the three, has the deepest Moho estimate at ~40 km from the PRFs and ~36 km from the SRFs. The estimated Moho depth for TGN19, which is the furthest to the south, is ~39 km from the PRFs and ~32 km from the SRFs. TGN18 is located between these two stations and has the shallowest PRF and SRF Moho estimates at ~32 km and ~28 km, respectively. The final stations in the northern group, TGN20 and TGN21, are located in the Central Ranges to the southeast of station TGN19, and have estimated Moho depths of ~34 km and ~32 km respectively.

LITHOSPHERE-ASTHENOSPHERE BOUNDARY DEPTH VARIATIONS FROM S WAVE RECEIVER FUNCTIONS

Interpretation of Receiver Functions

The lithosphere-asthenosphere boundary (LAB) results are drawn from S wave receiver functions, as P wave receiver functions are not able to resolve this deeper discontinuity. This is due to the fact that the P to s conversion at the LAB tends to be obscured by the arrival of P wave multiples and other converted P-phases in the wavetrain. As the S to p conversion at the LAB arrives ahead of the main S arrival and S multiples, it can be more readily isolated from the wavetrain (e.g. Kumar et al., 2007).

At the Taiwan orogen, the subducting Eurasian lithosphere dips to the east-southeast, and each of the earthquakes used in this study were located southeast of Taiwan in the Tonga-Fiji region. As a result, it was possible that rays useful for lithosphere-asthenosphere boundary depth estimation from these events may not be converted when crossing the impedance boundary at the base of the lithosphere beneath Taiwan, but instead would propagate through the slab itself. An inspection of raypaths using calculated angles of incidences and subducting slab geometry from tomography (Kuo-Chen et al., 2010) and seismicity (Wu et al., 2009) confirms that for the earthquakes used in this study, the up-going seismic rays were deep enough to pass underneath the subducting slab, not through it. In a similar study, Heit et al (2008) primarily utilized earthquakes from NW of the Andes subduction zone so that up-going rays came from the direction opposite subduction. Some earthquakes located SE of the Andes were also included and were stacked together with the events from the NW, suggesting that earthquakes from azimuths in line with the subduction direction, as were used in this study, may also provide coherent receiver function results.

Central Group

Lithosphere-asthenosphere boundary estimates for both the central and northern groups are given in Table 3. Profiles of the LAB estimates from S wave receiver functions for the central group are shown in Figure 15. A map of the estimated depth to the LAB for both groups is plotted in Figure 21.

The quality of the S wave receiver functions from the central group varies with station location across the island of Taiwan. Two stations located in the Central Ranges (TGC08 and TGC09) did not yield coherent LAB signals though the stations located on the Coastal Plan and Western Foothills give more convincing results. For stations TGC01 through TGC06, the up-going seismic waves sample the base of the Eurasian lithosphere. Stations TGC07 through TGC12 on the eastern side of Taiwan, where the up-going seismic waves sample the Philippine Sea Plate, also yielded receiver functions with more distinct LAB signals.

S wave receiver functions from the western stations in the central group indicate that the LAB becomes deeper from west to east across the Coastal Plain and Western Foothills. The LAB is estimated at approximately ~100 km deep beneath stations TGC01 and TGC03, and at approximately ~111 km deep at TGC04. These values presumably correspond to stable, un-deformed continental margin lithosphere, which has typical thicknesses of 100 to 125 km (Angus et al., 2006). Further east, the LAB is estimated at ~130 km at station TGC05, ~138 km at TGC06, and ~145 km at TGC07 and TGC08. Here the lithosphere-asthenosphere boundary is deepening as a result of the subduction of the Eurasian Plate. At station TGC09, the LAB signal is not as prominent, but the receiver function indicates LAB at ~165 km. Station TGC10 indicates an LAB depth of ~130 km, and at stations TGC11 and TGC12 the LAB is estimated at approximately ~120 km. Results from stations TGC07 through TGC12 suggest that the Philippine Sea Plate lithosphere has been thickened slightly from an

initial value of 80 to 90 km (Kawakatsu et al., 2009) during collision with the Eurasian continental margin.

Northern Group

S wave receiver functions from stations in the northern group also display a great deal of variability in the clarity of the LAB signal. The LAB beneath stations TGN01 and TGN02 is estimated at ~113 km, but the signal is weak at both stations. At station TGN03, the signal is more easily identified and indicates LAB at a depth of approximately 123 km. LAB signals for stations TGN04 and TGN05 are not as clear, but suggest LAB depths of ~129 km and ~119 km, respectively. TGN06 and TGN08 yield clearer LAB signals, with estimated LAB depth of ~123 km and ~137 km. The SRF for TGN09 is exceptionally noisy, despite the high number of events used, and only a tentative LAB depth estimate of ~141 km can be made.

Of the remaining TGN stations, robust LAB signals are only seen in SRFs from two stations. TGN18 indicates a LAB depth of ~107 km off the northeastern coast of Taiwan, south of Ilan. Southeast of this point, results from station TGN21 give an estimated LAB depth of ~105 km beneath offshore northeastern Taiwan, possible related to thinning near the Okinawa Trough. Estimated LAB depths for the remaining northern group stations are presented in Table 3.

Table 3. Lithosphere-asthenosphere boundary depth estimates from S wave receiver functions for seismic stations in the central and northern TAIGER groups.

Station	SRF LAB Estimate (km)	Number of Events Used
TGC01	102	19
TGC03	99	17
TGC04	111	13
TGC05	130	05
TGC06	138	11
TGC07	144	12
TGC08	145	06
TGC09	165	11
TGC10	130	19
TGC11	117	19
TGC12	125	16
TGN01	112	12
TGN02	114	13
TGN03	123	14
TGN04	129	13
TGN05	119	01
TGN06	123	04
TGN08	137	01
TGN09	141	15
TGN11	128	05
TGN12	100	11
TGN13	117	15
TGN14	98	12
TGN15	101	03
TGN16	132	08
TGN17	132	14
TGN18	107	12
TGN19	131	15
TGN20	132	19
TGN21	105	13

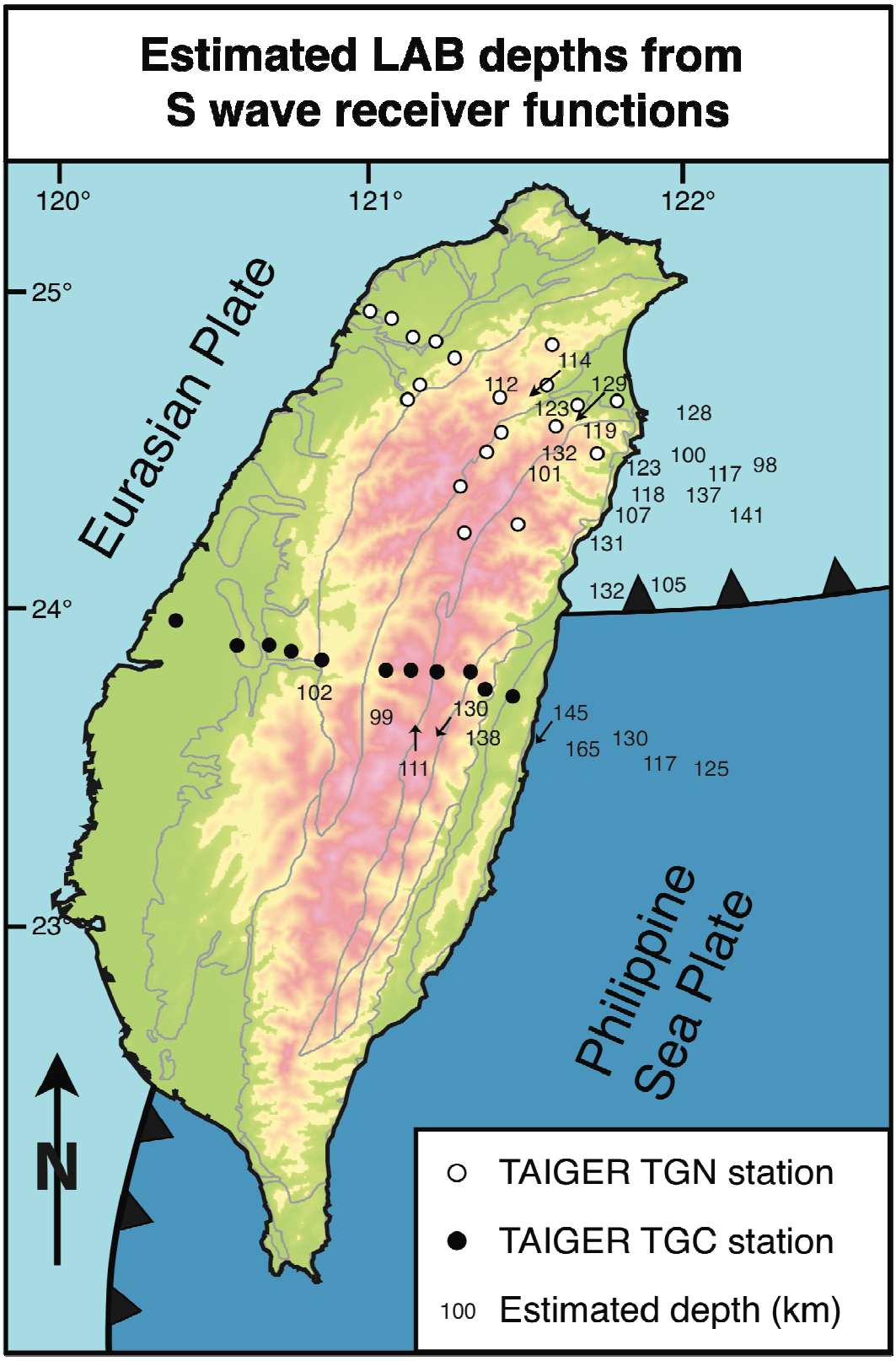
Estimated LAB depths from
S wave receiver functions
120°
121°
122°
25°
24°
23°
Eurasian Plate
Philippine
Sea Plate
N
114
112
129
123
128
119
132
100
101
123
117
98
118
137
107
141
131
132
105
102
99
130
138
111
145
165
130
117
125
TAIGER TGN station
TAIGER TGC station
100 Estimated depth (km)

Figure 21. Map of estimated Lithosphere-Asthenosphere Boundary (LAB) depths from S wave receiver functions for the northern and central groups. The numbers are plotted above the calculated 100 km depth piercing point for each station. A question mark (?) indicates a station where S wave receiver functions did not yield a clear LAB conversion signal.

DISCUSSION

Central Group

P wave receiver function results in western central Taiwan indicate the presence of a décollement at depth of 15 to 20 km. This feature is shallowest in the west and deepens eastward towards the core of the orogen, consistent with a thin-skinned model of deformation in this region. The furthest eastward station where the décollement is seen is TGC08, suggesting that a detachment persists to nearly 30 km deep beneath the Hsueshan and Western Central Ranges and at least as far east as 121.25º E longitude, approximately 18 km east of the Lishan Fault.

Beneath central Taiwan, however, P wave and S wave receiver functions indicate significant deepening of the Moho from west to east, strongly supporting an orogenic model that includes basement-involved faulting and crustal deformation in addition to a basal décollement (Figure 22). From the Coastal Plain in the west to the Western Foothills, the Moho increases in depth from approximately 30 km to nearly 40 km. The Moho continues to deepen, reaching its deepest point of approximately 50 km beneath the Central Ranges, and then becoming shallower again towards the east. This morphology suggests crustal thickening by approximately 60% beneath the Taiwan orogen. The thickening estimated here is consistent with thickening that occurs in numerical and geomechanical models of the Taiwan orogen (e.g. Kaus, 2008; Zhou et al., 2003). The eastern most seismic station in the central group, which presumably lies on the Philippine Sea Plate, indicates a much shallower Moho, at approximately 23 km for station TGC12. The thinner crust here is consistent with this station, along with TGC10 and TGC11, located to the east of the Longitudinal Valley, sampling the oceanic crust of the Philippine Sea Plate. However, a Moho depth of ~23 km suggests that the Philippine Sea Plate has also experienced some thickening during collision, as studies of the undeformed

Cross-section of Central Taiwan along the TAIGER TGC transect

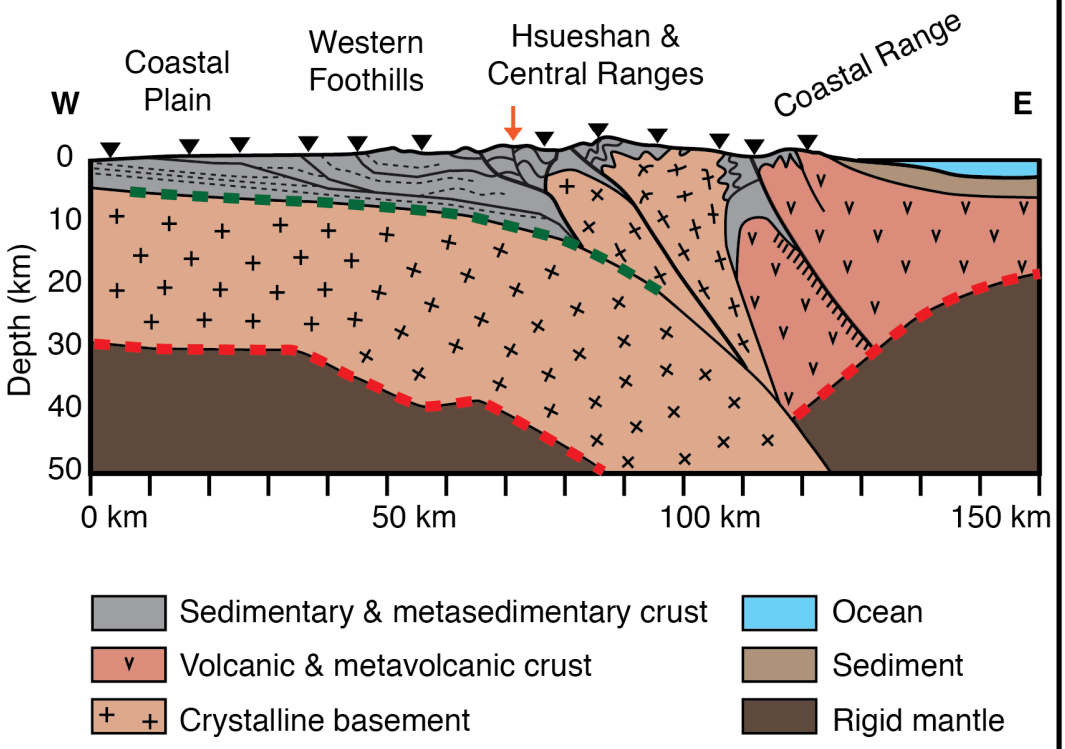

Adapted from Carena et al. (2002) and Chemenda et al. (2001)

Figure 22. Cross-section of central Taiwan along the TAIGER TGC transect. Broadband seismic stations from the TAIGER TGC group are plotted as black triangles. The orange arrow indicates the surface trace of the Lishan Fault. The dashed green line represents the basal décollement beneath western and central Taiwan. The dashed red line represents the estimated depth to the Moho from P wave receiver functions. The décollement is located at ~10 km depth beneath the Western Foothills, and increases in depth to the east. The décollement extends approximately 18 km east of the Lishan Fault and reaches a maximum imaged depth of ~20 km. The depth to the Moho for the Eurasian Plate is ~30 km beneath the Coastal Plain, and increases to ~50 km beneath the Hsueshan and Central Ranges in central Taiwan. In eastern Taiwan, the depth to the Philippine Sea Plate Moho increases towards the center of the island, from ~24 km off of the eastern coast to ~40 km beneath the Coastal Range. Structural interpretations for the Coastal Plain and Western Foothills in this cross-section were adapted from Carena et al. (2002), and structural interpretations for the Central Ranges and eastern were adapted from Chemenda et al. (2001).

Philippine Sea Plate suggest crustal thicknesses between 10 and 17 km (e.g. McIntosh et al., 2005; Wang et al., 2010).

The Moho depth estimates from the P wave receiver functions generally agree well with those S wave receiver functions for stations in the central group and are consistent with the results of several seismic tomography studies for the Taiwan orogen, including Rau & Wu (1995), Wang et al. (2006), and Wu et al. (2007), which indicate crustal thickening beneath Central Taiwan. Profile EW05, from tomography work conducted as part of the TAIGER project by Kuo-Chen et al. (2010), is shown in Figure 23 and depicts crustal thicknesses of 30 to 40 km in Western Taiwan, deepening to roughly 50 km beneath the Central Ranges, and significantly thinner crust of 30 km or less in the eastern part of the collisional system. These values match the Moho depth estimates from receiver functions in central Taiwan very well. Depth to the LAB is less defined in the tomography, however, the results from Kuo-Chen et al. (2010) depict a high velocity zone (~8.5 km/s) above the base of the Eurasian plate, in good agreement with the S wave receiver function results.

Northern Group

Receiver function results for northern Taiwan are more variable than the results from central Taiwan. High levels of noise from human activity in Northern Taiwan and relatively sparse data recovery for some northern stations contributed to the inconsistency of these results. Nonetheless, P and S wave receiver functions indicate that the depth to Moho increases eastward to depths of nearly 50 km across northern Taiwan, again suggesting significant crustal thickening beneath the Central Ranges. Profile EW06 (Figure 24) from the most-recent TAIGER tomographic study (Kuo-Chen et al., 2010) agrees well with the Moho depth estimates from this study, showing a slightly thickened crust beneath the Central Ranges in northern Taiwan.

S wave receiver functions for the central group plotted with tomography (Kuo-Chen et al. 2010) and seismicity (Wu et al. 2009)

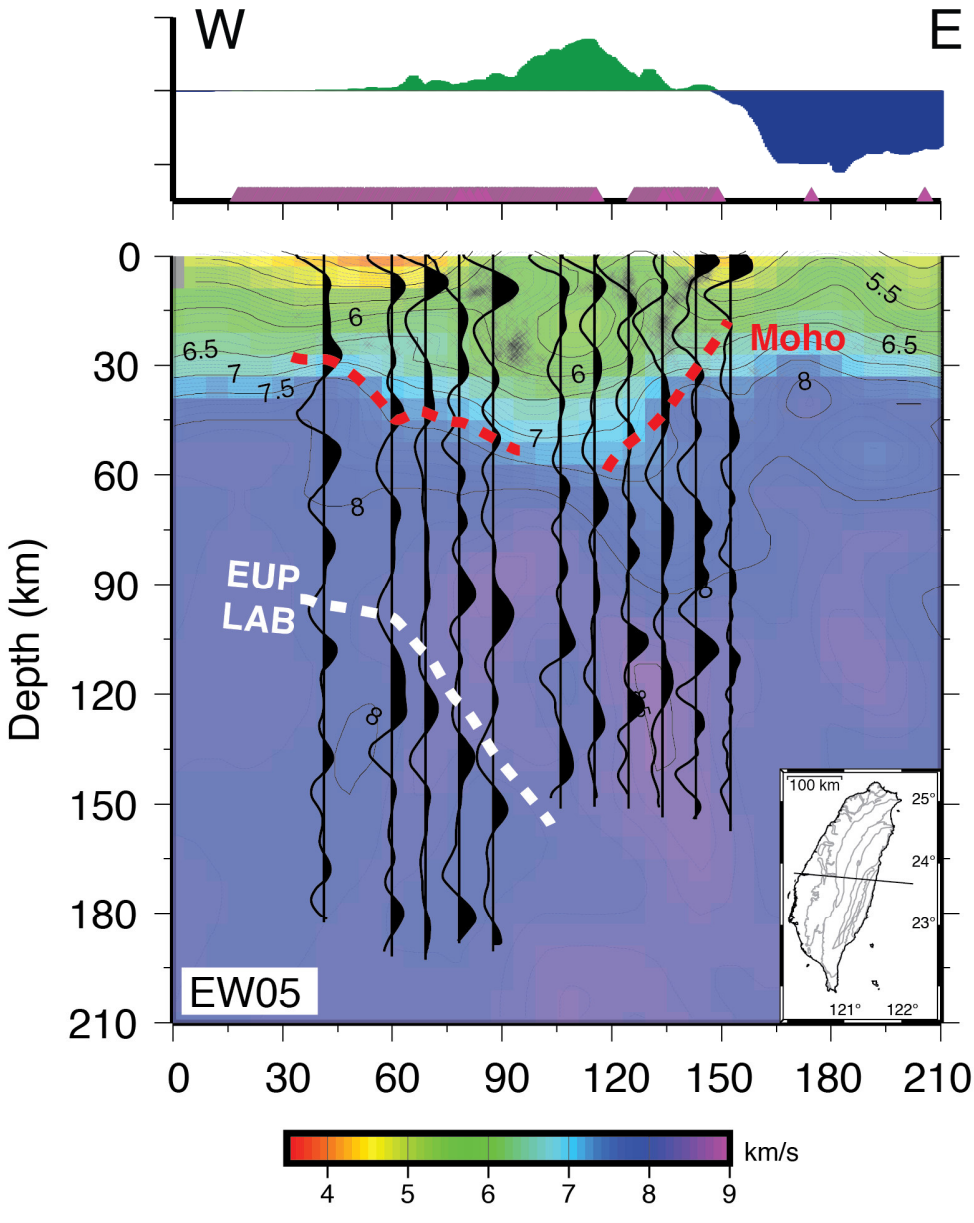

Figure 23. S wave receiver functions for the central group, plotted with tomography by the TAIGER group (Kuo-Chen et al., 2010). Moho depths estimated by receiver functions follow the topography of the base of the crust as delineated by the tomography at approximately 6.7 km/s. The base of the Eurasian lithosphere (EUP LAB) also follows the base of a high-velocity zone shown in the tomography. Both datasets indicate subduction of the Eurasian continental margin and development of a crustal root beneath the Central Ranges in central Taiwan. The traces are plotted at locations that correspond to the 35 km depth piercing points in order to facilitate comparison with the Moho depth estimates from the tomography. Consequently, the LAB depth estimates are plotted approximately 50 km to the left of the correct positions in the figure.

S wave receiver functions for the northern group plotted with tomography (Kuo-Chen et al. 2010) and seismicity (Wu et al. 2009)

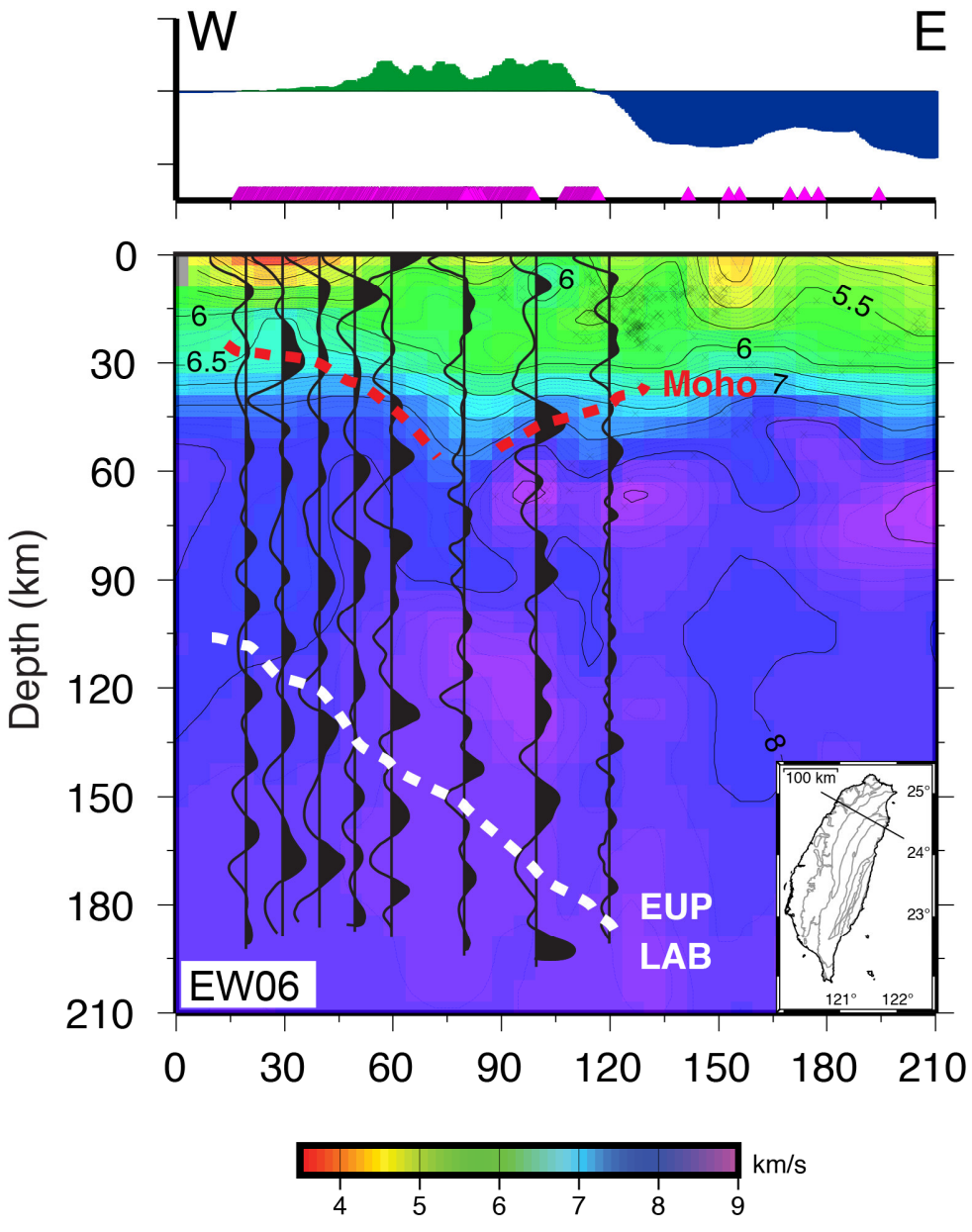

Figure 24. S wave receiver functions for the northern group, plotted with tomography by the TAIGER group (Kuo-Chen et al., 2010). Moho estimates from receiver functions agree with the tomography in showing thicker crust and a deeper Moho beneath central northern Taiwan. The traces are plotted at locations that correspond to the 35 km depth piercing points in order to facilitate comparison with the Moho depth estimates from the tomography. Consequently, the LAB depth estimates are plotted approximately 50 km to the left of the correct positions in the figure.

Lithosphere-asthenosphere boundary results from the S wave receiver functions are generally poor for the northern stations. Because all of the earthquakes used in the receiver function analyses were located to the southeast of Taiwan in the Tonga/Fiji region, it is likely that the complex plate geometries beneath the island affected the up-going seismic waves as they neared Taiwan. The steeply-dipping subduction of the Eurasian slab, the possible presence of increased melt due to propagation of the Okinawa Trough, and anisotropy in the rocks of the Central Ranges all contribute to the poor-quality of S wave receiver functions in this area. Further analysis using earthquakes located north to west of the seismic stations would bypass some of these factors by moving the piercing points of the up-going seismic waves away from the zone of maximum geometric complexity. Additionally, better constraints on the velocity structure of northern Taiwan, especially the localized influence of anisotropy that was beyond the scope of this study, could help to refine the estimates and clear up local variations in estimated depths.

CONCLUSIONS

The TAIGER broadband deployment provides a new seismic dataset with broad geographic coverage for a receiver function study to investigate the lithospheric structure. Working with this dataset, however, presented several challenges. Given the short duration of the TAIGER broadband seismic deployment, only a small group of seismic events suitable for receiver function analysis were recorded. Many of the stations were located in areas of high human activity, and the resulting noise levels made analysis and interpretation difficult or impossible for some stations.

P wave receiver functions indicate that the thrust décollement beneath the Western Foothills continues westward, penetrating the Hsueshan and Western Central Ranges at least as far as 121.25º E at 23.85º N. The fact that it cannot be traced further suggests that east of this region, deformation and crustal thickening is accommodated via steeply-dipping faults and/or ductile deformation. Results from both P and S wave receiver functions indicate that the Moho increases in depth beneath central Taiwan from the Coastal Plain on the western side of the island through the Hsueshan and Central Ranges, and then becomes shallower further to the east. From these results, a collisional model that incorporates a transition from thin-skinned collision in the west to thick-skinned collision beneath the Central Ranges seems most appropriate for the Taiwan orogen.

A similar morphology occurs in northwestern Taiwan, though the Moho does not appear to be as shallow beneath northeastern Taiwan. Results from S wave receiver functions from stations located on the Coastal Plain and in the Western Foothills in both central and northern Taiwan indicate deepening of the base of the Eurasian lithosphere from west to east, consistent with subduction of 100 to 120 km thick Eurasian lithosphere to the east beneath the Philippine Sea Plate.

WORKS CITED

Ai, Y., Chen, Q., Zeng, F., Hong, X. and Ye, W., 2007. The crust and upper mantle structure beneath southeastern China. Earth and Planetary Science Letters, 260: 549-563.

Al-Damegh, K., Sandvol, E. and Barazangi, M., 2005. Crustal structure of the Arabian plate: new constraints from the analysis of teleseismic receiver functions. Earth and Planetary Science Letters, 231(3-4): 177-196.

Ammon, C.J., 1991. The Isolation of Receiver Effects from Teleseismic P-Wave-Forms. Bulletin of the Seismological Society of America, 81(6): 2504-2510.

Angelier, J., 1986. Special Issue on Geodynamics of the Eurasia Philippine Sea Plate Boundary - Selected Papers from the Colloquium Held in Taiwan, ROC, March 28-30, 1984 - Preface. Tectonophysics, 125(1-3): R9-R10.

Angus, D.A. et al., 2009. Stratigraphy of the Archean western Superior Province from P- and S-wave receiver functions: Further evidence for tectonic accretion? Physics of the Earth and Planetary Interiors, 177: 206-216.

Angus, D.A., Wilson, D.C., Sandvol, E. and Ni, J.F., 2006. Lithospheric structure of the Arabian and Eurasian collision zone in eastern Turkey from S-wave receiver functions. Geophysical Journal International, 166(3): 1335-1346.

Armstrong, R.L., 1968. Sevier Orogenic Belt in Nevada and Utah. Geological Society of America Bulletin, 79: 429-458.

Barr, T.D. and Dahlen, F.A., 1989. Brittle Frictional Mountain Building .2. Thermal Structure and Heat-Budget. Journal of Geophysical Research-Solid Earth and Planets, 94(B4): 3923-3947.

Barr, T.D., Dahlen, F.A. and McPhail, D.C., 1991. Brittle Frictional Mountain Building .3. Low-Grade Metamorphism. Journal of Geophysical Research-Solid Earth and Planets, 96(B6): 10319-10338.

Barrier, E. and Angelier, J., 1986. Active Collision in Eastern Taiwan - the Coastal Range. Tectonophysics, 125(1-3): 39-72.

Biq, C.C., 1972. Dual Trench Structure in the Taiwan-Luzon region. Proc. Geol. Soc. China, 15: 65-75.

Bowin, C., Lu, R.S., Chaoshing, L. and Schouten, H., 1978. Plate Convergence and Accretion in Taiwan-Luzon Region. Aapg Bulletin-American Association of Petroleum Geologists, 62(9): 1645-1672.

Burdick, L.J. and Langston, C.A., 1977. Modeling crustal structure through the use of converted phases in teleseismic body-wave phases. Bulletin of the Seismological Society of America, 67(3): 677-691.

Carena, S., Suppe, J. and Kao, H., 2002. Active detachment of Taiwan illuminated by small earthquakes and its control of first-order topography. Geology, 30(10): 935-938.

Chai, B.H.T., 1972. Structure and Tectonic Evolution of Taiwan. American Journal of Science, 272(5): 389-&.

Chemenda, A.I., Yang, R.-K., Stephan, J.-F., Konstantinovskaya, E.A. and Ivanov, G.M., 2001. New results from physical modeling of arc-continent collision in Taiwan: evolutionary model. Tectonophysics, 333: 159-178.

Coward, M.P., 1983. Thrust tectonics, thin skinned or thick skinned, and the continuation of thrusts to deep in the crust. Journal of Structural Geology, 5(2): 113-123.

Crotwell, H.P., Owens, T.J. and Ritsema, J., 1999. The TauP Toolkit: Flexible Seismic Travel-time and Ray-path Utilities. Seismological Research Letters, 70: 154-160.

Dahlen, F.A., Suppe, J. and Davis, D., 1984. Mechanics of Fold-and-Thrust Belts and Accretionary Wedges - Cohesive Coulomb Theory. Journal of Geophysical Research, 89(NB12): 87-101.

Davis, D., Suppe, J. and Dahlen, F.A., 1983. Mechanics of Fold-and-Thrust Belts and Accretionary Wedges. Journal of Geophysical Research, 88(NB2): 1153-1172.

Font, Y., Kao, H., Liu, C.S. and Chiao, L.Y., 2003. A comprehensive 3D seismic velocity model for the eastern Taiwan-southernmost Ryukyu regions. Terrestrial Atmospheric and Oceanic Sciences, 14(2): 159-182.

Heit, B., Yuan, X.H., Bianchi, M., Sodoudi, F. and Kind, R., 2008. Crustal thickness estimation beneath the southern central Andes at 30 degrees S and 36 degrees S from S wave receiver function analysis. Geophysical Journal International, 174(1): 249-254.

Ho, C.S., 1986. A synthesis of the geologic evolution of Taiwan. Tectonophysics, 125: 1-16.

Ho, C.S., 1988. An introduction to the geology of Taiwan, technical report, 2nd edition, Central Geological Survey, Ministry of Economic Affairs, Taipei.

Hou, C.-S. et al., 2009. The crustal deformation of the Ilan Plain acted as a westernmost extension of the Okinawa Trough. Tectonophysics, 466: 344-355.

Kao, H., Shen, S.S.J. and Ma, K.F., 1998. Transition from oblique subduction to collision: Earthquakes in the southernmost Ryukyu arc-Taiwan region. Journal of Geophysical Research-Solid Earth, 103(B4): 7211-7229.

Kaus, B.J.P., Steedman, C., Becker, T.W., 2008. From passive continental margin to mountain belt: Insights from analytical and numerical models and application to Taiwan. Physics of the Earth and Planetary Interiors, 171: 235-251.

Kawakatsu, H. et al., 2009. Seismic Evidence for Sharp Lithosphere-Asthenosphere Boundaries of Oceanic Plates. Science, 324: 499-502.

Keefer, W.R. and Love, J.D., 1963. Laramide vertical movements in central Wyoming. University of Wyoming Contributions to Geology, 2(1): 47-54.

Kennett, B.L.N. and Engdahl, E.R., 1991. Traveltimes for Global Earthquake Location and Phase Identification. Geophysical Journal International, 105(2): 429-465.

Kim, K.-H., Chiu, J.-M., Kao, H., Liu, Q. and Yeh, Y.-H., 2004. A preliminary study of crustal structure in Taiwan region using receiver function analysis. Geophysical Journal International, 159: 146-164.

Kind, R. and Vinnik, L.P., 1988. The Upper-Mantle Discontinuities Underneath the Grf Array from P-to-S Converted Phases. Journal of Geophysics-Zeitschrift Fur Geophysik, 62(3): 138-147.

Kumar, P. et al., 2005a. The lithosphere-asthenosphere boundary in the North-West Atlantic region. Earth and Planetary Science Letters, 236(1-2): 249-257.

Kumar, P., Kind, R., Priestley, K. and Dahl-Jensen, T., 2007. Crustal structure of Iceland and Greenland from receiver function studies. Journal of Geophysical Research-Solid Earth, 112(B3).

Kumar, P., Yuan, X., Kind, R. and Kosarev, G., 2005b. The lithosphere-asthenosphere boundary in the Tien Shan-Karakoram region from S receiver functions: Evidence for continental subduction. Geophysical Research Letters, 32(7).

Kuo-Chen, H. et al., 2010. 3D Vp and Vs Lithospheric Structures under the Taiwan Orogen: TAIGER project. American Geophysical Union, Fall Meeting 2010.

Lallemand, S., Font, Y., Bijwaard, H. and Kao, H., 2001. New insights on 3-D plates interaction near Taiwan from tomography and tectonic implications. Tectonophysics, 335: 229-253.

Lallemand, S.E., Liu, C.S. and Font, Y., 1997. A tear fault boundary between the Taiwan orogen and the Ryukyu subduction zone. Tectonophysics, 274(1-3): 171-190.

Langston, C.A., 1978. Structure under Mt Rainier, Washington, Inferred from Teleseismic Body Waves. Transactions-American Geophysical Union, 59(12): 1142-1142.

Lewis, S.D. and Hayes, D.E., 1983. The tectonics of northward propagating subduction along eastern Luzon, Philippine Islands. In: D.E. Hayes (Editor), The Tectonic and Geologic Evolution of Southeast Asian Seas and Islands: Part 2, Geophysical Monograph Series. AGU, Washington, D.C., pp. 57-78.

Li, X., Kind, R., Yuan, X., Wolbern, I. and Hanka, W., 2004. Rejuvenation of the lithosphere by the Hawaiian plume. Nature, 427(6977): 827-829.

McIntosh, K. et al., 2005. Crustal-scale seismic profiles across Taiwan and the western Philippine Sea. Tectonophysics, 401: 23-54.

Okaya, D.A. et al., 2009. Joint passive/controlled source seismic experiment across Taiwan. Eos, Transactions American Geophysical Union, 90(34): 289.

Rau, R.J. and Wu, F.T., 1995. Tomographic imaging of lithospheric structures under Taiwan. Earth and Planetary Science Letters, 133: 517-532.

Stammler, K., 1993. Seismichandler Programmable Multichannel Data Handler for Interactive and Automatic Processing of Seismological Analyses. Computers & Geosciences, 19(2): 135-140.

Suppe, J., 1981. Mechanics of mountain building and metamorphism in Taiwan. Geol. Soc. China, Mem. 4: 67-89.

Suppe, J. and Namson, J., 1979. Fault-bend origin of frontal folds of the western Taiwan fold-and-thrust belt. Pet. Geol. Taiwan, 16: 1-18.

Taylor, B. and Hayes, D., 1983. Origin and history of the South China Sea Basin. The Tectonic and Geologic Evolution of Southeast Asian Seas and Islands, Part 2, AGU Geophysical Monograph, 27: 23-56.

Teng, L.S., 1990. Geotectonic evolution of late Cenozoic arc-continent collision in Taiwan. Tectonophysics, 183(1-4): 57-76.

Vinnik, L.P., 1977. Detection of Waves Converted from P to Sv in Mantle. Physics of the Earth and Planetary Interiors, 15(1): 39-45.

Wang, Y.-J., Ma, K.-F., Mouthereau, F. and Eberhart-Phillips, D., 2010. Three-dimensional Qp- and Qs-tomography beneath Taiwan orogenic belt: implications for tectonic and thermal structure. Geophysical Journal International, 180(2): 891-910.

Wang, Z., Zhao, D.P., Wang, J. and Kao, H., 2006. Tomographic evidence for the Eurasian lithosphere subducting beneath south Taiwan. Geophysical Research Letters, 33(18).

Wu, F.T., Chang, C.S. and Wu, Y.M., 2004. Precisely relocated hypocentres, focal mechanisms and active orogeny in Central Taiwan. In: J. Malpas, Fletcher, C.J.N., Ali, J.R., Aitchison, J.C. (Editor), Aspects of the Tectonic Evolution of China. Geological Society, London, pp. 333-354.

Wu, F.T., Liang, W.-T., Lee, J.-C., Benz, H. and Villasenor, A., 2009. A model for the termination of the Ryukyu subduction zone against Taiwan: A junction of collision, subduction/separation, and subduction boundaries. J. Geophys. Res., 114(B7): B07404.

Wu, F.T., Rau, R.-J. and Salzberg, D., 1997. Taiwan orogeny: thin-skinned or lithospheric collision? Tectonophysics, 274: 191-220.

Wu, Y.-M. et al., 2007. Seismic tomography of Taiwan: Improved constraints from a dense network of strong motion stations. Journal of Geophysical Research, 112.

Yu, S.B., Chen, H.Y. and Kuo, L.C., 1997. Velocity field of GPS stations in the Taiwan area. Tectonophysics, 274(1-3): 41-59.

Yu, S.B., Kuo, L.C., Punongbayan, R.S. and Ramos, E.G., 1999. GPS observation of crustal deformation in the Taiwan-Luzon region. Geophysical Research Letters, 26(7): 923-926.

Yuan, X., Ni, J., Kind, R., Mechie, J. and Sandvol, E., 1997. Lithospheric and upper mantle structure of southern Tibet from a seismological passive source experiment. Journal of Geophysical Research-Solid Earth, 102(B12): 27491-27500.

Yuan, X.H., Kind, R., Li, X.Q. and Wang, R.J., 2006. The S receiver functions: synthetics and data example. Geophysical Journal International, 165(2): 555-564.

Zhou, D., Yu, H.-S., Xu, H.-H., Shi, X.-B. and Chou, Y.-W., 2003. Modeling of thermo-rheological structure of lithosphere under the foreland basin and mountain belt of Taiwan. Tectonophysics, 374: 115-134.

Appendix: Data Processing

The SeismicHandler software package (Stammler, 1993) provides several options for rotating data into ray coordinate reference frame, depending on the amount of metadata contained in the header files. In addition to the latitude and longitude of the seismic station (φ_0, λ_0), the azimuth and the angle of incidence of the up-going ray are also required to rotate to the RCRF. When the required information is not included in the header, it can be determined using parameters calculated in the TauP software (Crotwell et al., 1999). The "taup_time" function yields specific phase travel times as well as angular distance (Δ) and ray parameter (p) values for each earthquake/station pair. Azimuth (α) from station to epicenter is found using the following formula:

$$\sin(\alpha) = [\cos(\varphi) \sin(\lambda - \lambda_0)] / \sin(\Delta)$$

where φ is the latitude of the epicenter, λ is the longitude of the epicenter, and λ_0 is the longitude of the station. Using the calculated ray parameters, the angle of incidence, i, is found using the following formula:

$$p = \sin(i) / v$$

where p is the seismic ray parameter, and v is the velocity of the phase of interest. In this study, the phase velocities used are from the IASP-91 model (Kennett and Engdahl, 1991).

Following the rotation, the data are high-pass filtered at either 10 seconds or 20 seconds, as needed. Next, a window surrounding the phase of interest is cut from the rotated and filtered data. For the PRFs, the window begins approximately 200 seconds prior to the estimated P arrival and ends roughly 100 seconds before the S phase arrivals. For the SRFs, the window begins ~100 seconds before the estimated S arrival and ends just before the arrival of the surface wave package. A spiking deconvolution, which effectively produces a narrower, higher amplitude wavelet, is then applied to the data, with the deconvolution window of 90 to 100 seconds centered on the arrival of the

primary phase of interest. Deconvolution emphasizes the phases of interest, making them easier to identify on individual datasets. The records are again clipped to ten seconds prior to the main arrival in order to facilitate stacking.